STUDY OF JET AND MISSING TRANSVERSE ENERGY PERFORMANCE IN DIJET EVENTS WITH ATLAS DATA

by

SUSHMITA SAHU

Presented to the Faculty of the Graduate School of
The University of Texas at Arlington in Partial Fulfillment
of the Requirements
for the Degree of

MASTER OF SCIENCE IN PHYSICS

THE UNIVERSITY OF TEXAS AT ARLINGTON

December 2011

ACKNOWLEDGEMENTS

First and foremost, I would like to thank my Supervising Advisor Dr Kaushik De for his unconditional support ,motivation and mentoring. I wish to thank Dr Giulio Usai for his constant guidance and advice. I would like to thank my Graduate Advisor Dr Qiming Zhang for guiding me throughout my Master's course. I thank Dr Kaushik De, Dr Giulio Usai and Dr Qiming Zhang for being in my thesis committee as well.

I would like to thank UTA High Energy Physics Professors for their support. Many thanks to Dr Mark Sosebee, Dr Rishiraj Pravahan and Dr Alden Stradling for their help and support whenever needed.

I also thank the UTA Physics Department for their support. I express my deepest gratitude to all my teachers during my Master's course. Finally much thanks I owe to my parents for their everlasting love and support and to my husband for being by my side always.

November 17, 2011

ABSTRACT

STUDY OF JET AND MISSING TRANSVERSE ENERGY PERFORMANCE IN DIJET EVENTS WITH ATLAS DATA

Sushmita Sahu, M.S.

The University of Texas at Arlington, 2011

Supervising Professor: Dr Kaushik De

The Large Hadron Collider(LHC) is the world's largest particle collider at CERN, Geneva, operating at a center of mass energy of 7 TeV . The Toroidal LHC Apparatus (ATLAS)is one of two general purpose detectors at the LHC. It is responsible for measuring particles produced in proton-proton collisions and to search for new particles.

The High Energy Physics group at UTA has been involved with designing, construction and commissioning of the ATLAS Tile Calorimeter, one of the sub-detectors of ATLAS. One of the components of Tile Cal, the Intermediate Tile Calorimeter (ITC) was constructed at UTA. UTA has been actively involved with the performance and calibration of the ITC.

This thesis analyzes jet calibration and performance in the central region of the Calorimeter for di-jet events collected by ATLAS in 2011. The thesis also studies the performance and resolution of missing transverse energy, E_T^{miss}. The performance of the Calorimeter for different regions of pseudo-rapidity and for varying transverse

momentum have been studied in detail. This dissertation will in addition focus on the performance and calibration of the ITC region.

TABLE OF CONTENTS

LIST OF ILLUSTRATIONS

LIST OF TABLES

CHAPTER 1

INTRODUCTION

This chapter gives a brief introduction of the standard model of physics,which describes the fundamental particles and the various fundamental forces or interactions. The chapter also provides a brief overview of the LHC collider.

Experiments have shown that all the matter is made of 12 fundamental particles called *fermions* bounded by different interactions by the exchange of force mediating particles called bosons. The "Standard Model" of Particle Physics formulated in the middle of 1970s describes the behavior of all particles based on quantum field theory.

1.1 Standard Model

The standard model describes the elementary particles and the electromagnetic, weak and strong interactions involving the exchange of gauge bosons based on the quantum field theory[4, 5]. The gravity as the fourth known interaction is not included in the standard model and is much weaker then the other three forces.

1.1.1 Particles

All the particles of the standard model are shown in Figure 1.1: the first three columns are fermions, the last column are gauge bosons.

- Fermions: The three columns of fermions represent three generations of matter. Each generation has four fermions. The charge and spin of the corresponding particles across the three generations remain same while the mass increases with each generation. The top which is the third generation up quark has the

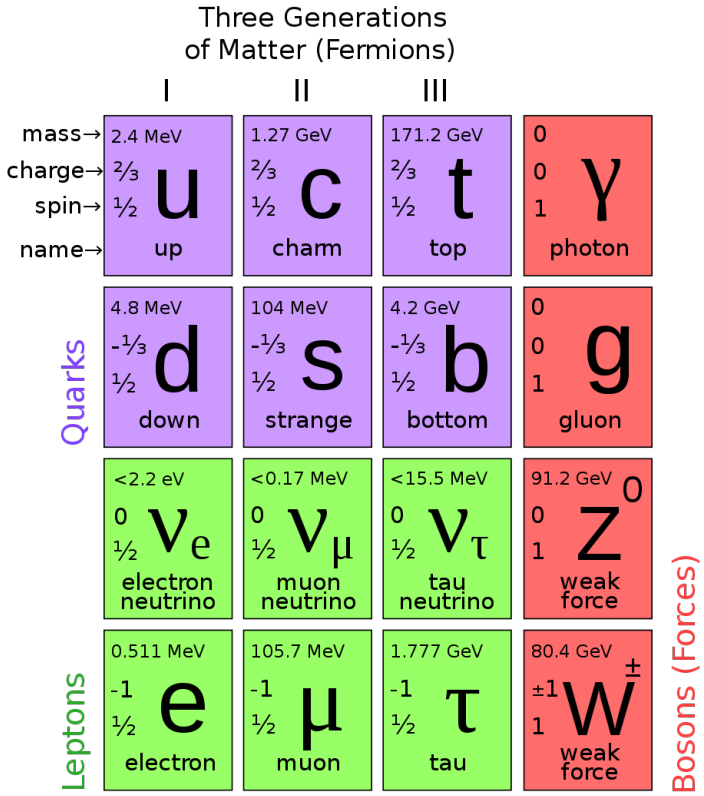

Figure 1.1. Standard model of elementary particles.

highest mass, comparable to that of a heavy atom. All the 12 fermions of the SM have their corresponding antifermion, with all identical properties except for the charge which is opposite. All the fermions are spin 1/2 particles. According to the spin-statistics theorem, fermions respect the Pauli exclusion principle.

The six quarks(up,down,charm,strange,top,bottom) carry color charge and interact via the strong interaction. The quarks are bound to each other by color confinement resulting in color neutral composite particles called hadrons. When hadrons contain a quark and an antiquark they are called mesons, while those containing three quarks are called baryons.

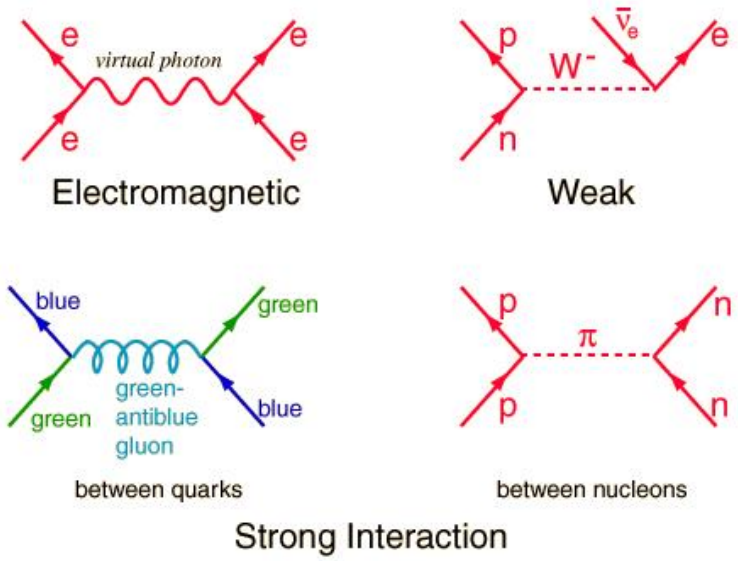

Figure 1.2. The Bosons and the interactions.

The remaining six fermions are colorless and called leptons. The three neutrinos are chargeless , and experience only the weak nuclear force. These are hence difficult to detect.

- Gauge Bosons: They are the force-mediating particles. All the gauge bosons have a spin of 1. Photons mediate the electromagnetic force between electrically charged particles. The photon is massless. The gluons mediate the strong interaction between color charged particles. Gluons are massless as well. The W^+, W^- and Z bosons mediate the weak interactions between quarks and leptons. They are very massive. W^{+-} carry a charge of +1 and -1, while the Z is electrically neutral.
- Higgs boson: The higgs boson is a hypothetical massive elementary particle which hasn't been observed yet. It is a key building block in the standard model. Since it has integer spin, it is called boson. Higgs is a scaler, i.e. spin 0.

1.1.2 Interactions

There are four fundamental interactions(forces) between particles. Mathematically the interactions are described as gauge field theory using symmetry groups $U(1) \times SU(2) \times SU(3)$[6].

- Electromagnetic Interaction: The electromagnetic force causes like-charged objects to repel and oppositely-charged objects to attract. The mediator of this force is the photon. Though it is a long distance interaction, the strength decreases with the square of distance. Symmetry group U(1) represents electromagnetic interaction. The coupling constant of the electromagnetic interaction is

$$\alpha = \frac{e^2}{4\pi hc} \cong 1/137 \tag{1.1}$$

- Strong Interaction: The strong interaction was identified with the nuclear interaction which acts between quarks. It is a short distance interaction occurring within $10^{-15}m$ and is represented by the gauge group $SU(3)_c$. This group symmetry states that there are three different charge eigenstates of the quarks. The eigenstates are represented by the three colors red, green and blue. The theory of the interaction is called quantum chromodynamics(QCD). The strong interaction coupling constant α_s essentially depends on the momentum transfer Q^2. At low Q^2(which means De Broglie law at large distances), α_s becomes large. Because of this quarks can not be observed as free particles but are bound as hadrons. If two quarks are separated from each other, the gluon field energy become high enough to create quark-antiquark pair. This phenomenon happens at high energy collisions with outgoing quarks and gluons and is called hadronization.

- Weak Interaction: The weak interaction governs certain radioactive element and also the decay of particles into lighter ones and acts upon all quarks and leptons, including those with no electric charge. It is the shortest distance interaction happening within 10^{-18}m.Above the unification energy, the weak and the electromagnetic force merge into a single electroweak force.The weak eigenstates of the quarks differ from their mass eigenstates. For this reason, the weak interaction can transform quarks from one generation into those of another. The symmetry group SU(2) represents the weak interaction which has three gauge fields resulting three vector bosons W^+, W^- and Z.

1.2 The p-p collision at LHC

The CERN large Hadron Collider, which is the largest hadronic collider in the world provides proton - proton collisions at a centre-of-mass energy of 7 TeV[7]. The total inelastic proton-proton cross-section is about 80 mb(1 barn=1024 cm^2 is a unit used in HEP) at the maximum LHC centre-of-mass energy of $\sqrt{s} = 14$ TeV. The number of interaction events produced per second is referred as the event rate R where

$$R = \sigma \times L = 80mb \times 10^{34} cm^{-2} s^{-1} \approx 10^9/s \tag{1.2}$$

The events can be categorized into two classes:

- Minimum bias events: Most of the events in the proton-proton collisions are due to large distance collisions between the two. This results in small momentum transfer(called *soft collisions*)[8]. The final state particles have large longitudinal momentum but small transverse momentum(p_T) relative to the beam direction. These soft interactions' final state are called minimum bias events.
- Hard Scattering events The proton consists of partons(quarks and gluons). So for the monochromatic proton beams, occasionally head on collision occurs

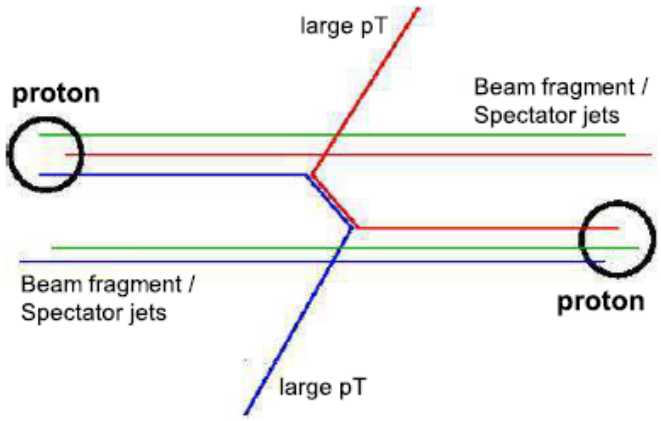

Figure 1.3. A high p_T pp collision.

between two partons. These collisions are at small distance hence have large momentum transfers(called *hard scattering*). The final state particles can be produced at large angles with respect to beam lines. Massive particles can be created in these collisions. Although these events are rare compared to soft interactions , they are interesting physics events.

For both the above mentioned type of events, the transverse momentum(the one perpendicular to beam axis) of the incident quarks and gluons are negligible and the total transverse momentum in the initial state is approximately zero. Following the conservation of momentum, the total transverse momentum in the final state must be zero. But the measured transverse momentum(or transverse energy)in the final state may be non negligible because of various reasons like

- non interacting or weakly interacting particles usually escape the detection(neutrinoes)
- particles absorbed in regions of detector not active: dead material and other regions with detector problems
- limited acceptance of the detector where the particles with small angles can escape detection

- other particles produced in secondary collisions occuring at same time(pile-up).

This missing transverse momentum called often "Missing Transverse Energy". E_T^{miss} is therefore the most important signature for non-interacting particles like neutrinos or unknown particles that are not yet detected. Thus E_T^{miss} needs to be evaluated with utmost precision.

CHAPTER 2

ATLAS DETECTOR AT LHC

This chapter describes the ATLAS Detector detailing all the detecting systems. It is one of the four particle detectors designed to measure different types of new physics that might become detectable in the energetic collisions of the LHC. A brief introduction of the LHC is given in the chapter. This chapter also describes the reconstruction of physics objects with four-momenta as they are used in analyses; i.e. jets, electrons, muons and missing transverse energy.

2.1 Large Hadron Collider

The LHC is a circular proton-proton and heavy ion collider located at CERN, Geneva[9]. It is the world's largest and highest-energy particle accelerator. It is constructed in a tunnel about 100 m underground with a circumference of 26.7 km. LHC is designed to accelerate protons to an energy of 7 TeV at a maximum luminosity of $10^{34} cm^{-2} s^{-1}$. It also provides pb - pb collisions with a center of mass energy of 5.5 TeV and luminosity of $10^{27} cm^{-2} s^{-1}$. The LHC started operating from November 2009 at an initial energy of 450GeV per beam. After a brief shutdown in winter 2009, the LHC was restarted in March 2010, operating at half its designated energy of 3.5 TeV per beam. By mid 2011, LHC has crossed the milestone of $5 fb^{-1}$(5 inverse femtobarn) collisions, which correspond to 3.4×10^{14} collisions.

The counter rotating beams of the LHC cross each other at four points along the tunnel. It is at these points where the four detectors : ALICE(A Large Ion Collider Experiment)[10], ATLAS(A Toroidal LHC ApparatuS) ,CMS(Compact Muon

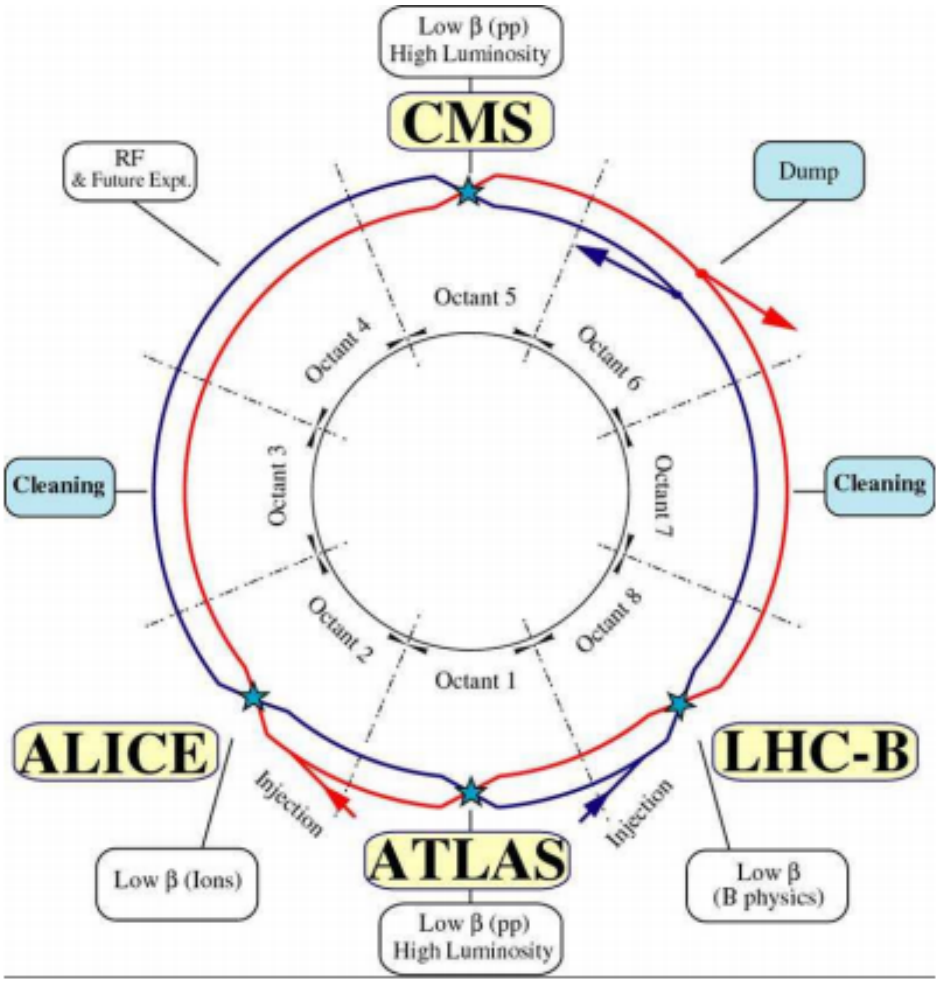

Figure 2.1. The LHC with the four main detectors including ATLAS.

Solenoid Experiment)[11] and LHCb(the Large Hadronic Collider beauty experiment)[12] are located. The CMS is a general purpose detector like ATLAS, the ALICE is designed to study heavy ion Pb-Pb collisions while the LHCb studies the B quark physics. Fig 2.2 shows the LHC with pre-accelerators : the linear accelerator (LINAC), the Proton Synchrotron Booster (PSB), the Proton Synchrotron (PS) and the Super Proton Synchrotron (SPS). Hydrogen atoms are stripped to get the protons which are then accelerated to 50 MeV in the LINAC. They are subsequently accelerated to 1 GeV, 26 GeV and 450 GeV by the pre-accelerators PSB, PS and SPS in that

order. The protons are constrained in branches upto 10^{11} protons each and with a 25ns bunch separation applied. The bunches are injected into the LHC in clockwise and counter clockwise direction by the SPS. The LHC then accelerates the photon to a 7 TeV energy. The event rate that is the number of produced events is given by :

$$R = \sigma \times L \tag{2.1}$$

where σ is cross section of the event and L is the luminosity of LHC. The luminosity L is defined as :

$$L = \frac{N_b^2 n_b f_{rev} \gamma_r}{4\pi\sigma_t^2} \tag{2.2}$$

where

- N_b : number of particles per bunch($\sim 10^{11}$ for high luminosity, $\sim 10^{10}$ for low luminosity)
- n_b : number of bunches per beam (2808)
- f_{rev} : revolution frequency (40 MHz)
- γ_r : relativistic gamma factor
- σ_T : transverse beam size (16.7 μ m)

2.2 ATLAS Detector

ATLAS is the largest detector of LHC, with a length of 44m and diameter of 25m[1]. The magnetic fields are generated by large toroid coils and a central solenoid. Even though its performances is optimized for the Higgs search, it can cope with the study of a variety of phenomena. It has three detecting regions: inner tracking detector, calorimeters and the muon spectrometer. The detectors with the sub-detectors are configured in concentric circles around the beam axis, each of them designed for detecting specific particles. A detailed description of the detector can be found in [11].

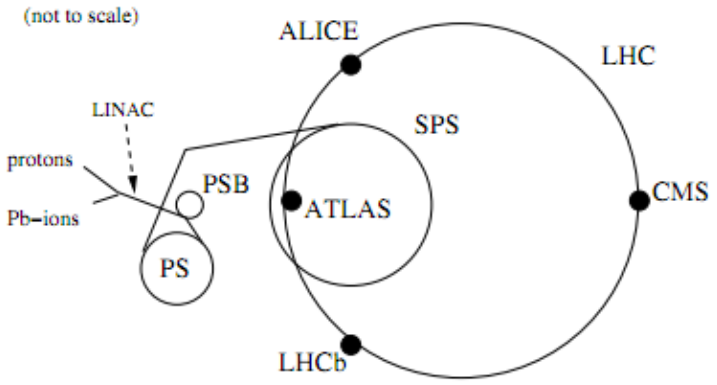

Figure 2.2. Schematic view of the particle accelerators and detectors at CERN.

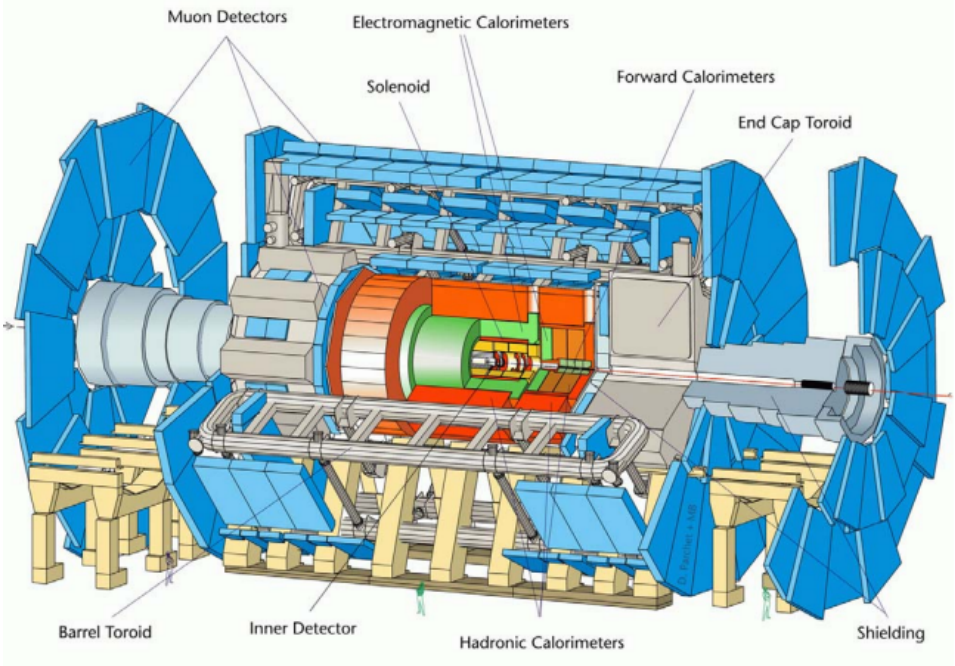

Figure 2.3. ATLAS Detector[1].

2.2.1 Detector Coordinate System

The longitudinal z axis runs parallel to the beam line in counter-clock wise direction.The half of the detector that corresponds to positive values of z is referred to as side A and the other half as side C. The x-axis points to the center of the LHC ring and the y-axis points upwards to the surface.The xy-plane is referred to as the transverse plane.

Each sub-detectors in ATLAS consists of concentric cylindrical layers around the beam axis, the barrel component, and two endcaps formed by disks perpendicular to the z-axis on each side of the interaction point. The radial distance is $R == \sqrt{x^2 + y^2}$. The azimuthal angle ϕ is the angle with the positive x-axis and ranges from $[-\pi, \pi]$. The polar angle θ is the angle with the positive z-axis and ranges from $[0, \pi]$. The polar angle is replaced by *pseudo-rapidity* η where $\eta = \ln \tan \theta/2$. Since *pseudo-rapidity* is an invariant quantity and distributes the transverse energy roughly evenly, hence it is preferred. The projection of momentum and energy in the transverse plane i.e. transverse momentum p_T and transverse energy E_T are used to describe the particle properties since they are conserved in collision.

2.2.2 General Layout

An ATLAS Detector is primarily made of sub-detectors configured in concentric layers around the beam axis. The detectors track the charged particles which leave traces in the detector. The calorimeter traces energy of all particles except muons and neutrinos. While the muon is detected in the Muon Spectrometer , the neutrino leaves the detector completely undetected.

As referred to figure 2.3 , The ATLAS Detector consists of 4 main components:

- Inner Detector: It is enclosed in the magnetic field of the solenoid and measures momentum of each charged particle. It consists of the Pixel Detector, Semiconductor tracker(SCT), Transition Radiation Tracker(TRT)
- Calorimeter: It measures the particle energies. The calorimeter is further divided into electromagnetic and hadronic calorimeter
- Muon Spectrometer: This measures the tracks of muons in the magnetic field of the toroid.
- Magnet System: It is a set of solenoid and toroidal magnet system and bends charged particles for momentum measurement.The central solenoid surrounds the inner detector and produces magnetic field parallel to the beam.The toroids provide the magnetic field to the Muon Spectrometer.

Figure 2.4 illustrates the different calorimeters with the η coverage in each part of detector.

2.2.3 Inner Detector

The inner detector provide the measurements of charged particle tracks. This is necessary for reconstruction of the charge of the particles and the momentum as well as the reconstruction of secondary vertices. It identifies the charged particle using the charge/mass ratio from the track and the distance from the particles' originating point to the interaction point. The inner detector is closest to the beam where particle density is largest, hence high granularity and good radiation tolerance are required. It is contained within a cylinder of length 3.5 m and of radius 1.2 m within a selenoidal magnetic field of 2T. The inner detector consists of three tracking devices:the *pixel detector*, the *semi-conductor tracker* (SCT) and the *transition radiation tracker* (TRT). Pixel is the innermost one, while the SCT lies between the Pixel and TRT. The inner

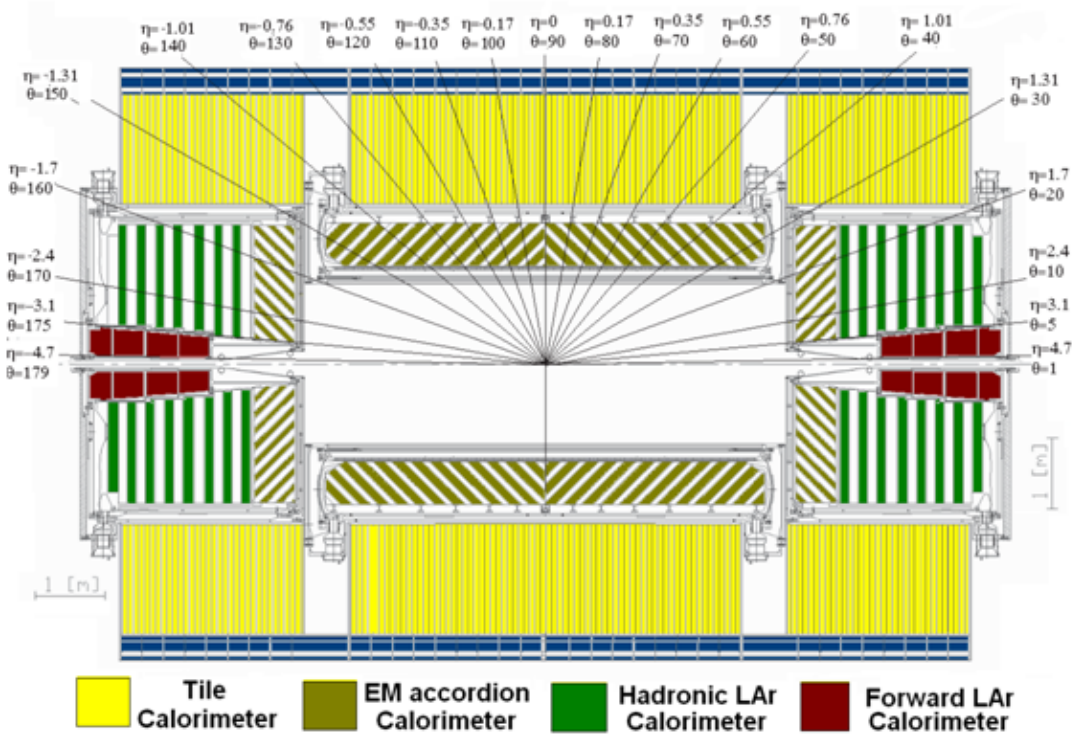

Figure 2.4. The Calorimeter with detailed η coverage.[2].

detector covers the pseudorapidity upto $|\eta| < 2.5$. All the sub-detectors are composed of barrel and end-caps to get maximum geometry coverage[13].

2.2.3.1 The Pixel Detector

The pixel detector comprises of a cylinder and several disks made up of 140 million silicon pixels measuring 50 to 300 μm along each side. They mainly contribute to precise identification of the primary vertex and secondary vertices. This detector gives the highest spatial resolution for tracks and vertices. The size of pixels is therefore kept very small giving a granularity of $50 \times 40\mu m^2$ in a total number of $\sim$ 80.4 million pixels.There are three barrel pixel layers of radius 50.5, 88.5 and 122.5 mm and six end-cap disks.The innermost B-layer enhances the ability to identify

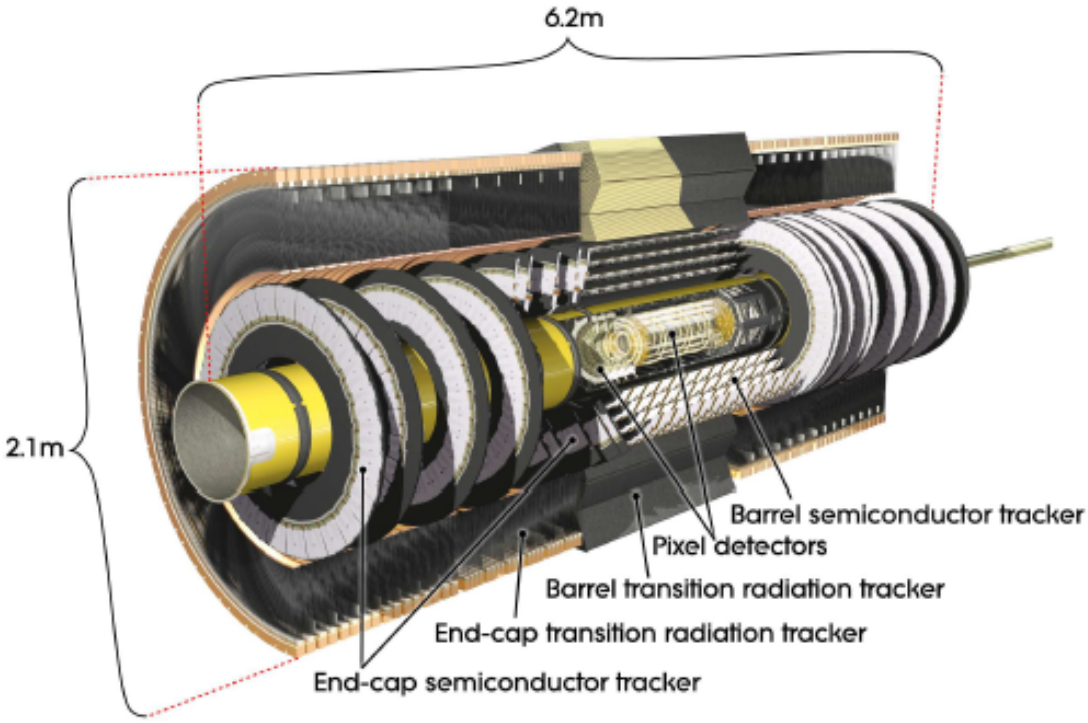

Figure 2.5. Inner detector[1].

secondary vertices for B-tagging and is exposed to very high radiation level. To reduce damages due to radiation and to increase performance , the detector is maintained at at temperature between -5 and -10^{o}C. Also the B-Layer is designed to be removable to repair radiation damage.

When charged particle passes through, electron-hole pairs are generated in the silicon, thereby generating a current which is read by the Pixel Detector. The intrinsic resolution of the pixel detector is $10\mu m$ and $115\mu m$ in the transverse and longitudinal dimensions respectively.

2.2.3.2 The semi-conductor tracker

The SCT has eight barrel layers and nine end-cap disks on either side. It is similar to the Pixel Detector except that because of low particle density, the silicon strips

are long and narrow. As the strips have a larger surface area than the pixels, this type of detector is less precise than the pixel detector but is less costly. Because the SCT measures the track over a much longer distance than the Pixel, it provides a better transverse momentum than the Pixel. It also provides more sampling points that the Pixel. The tracks can be distinguished if separated by more than $\sim 200\mu m$. The intrinsic accuracy of the SCT in the barrel region is $17\mu m$ in $r-\phi$ and $580\mu m$ in z. The accuracy is $17\mu m$ in $r-\phi$ and $580\mu m$ in r, for the end-cap disks.

2.2.3.3 The transition radiation tracker

The outermost component of Inner detector , the TRT consists of gaseous straw tubes interleaved with transition radiation material. The employed mixture of gases is 70% Xe, 20% CO_2 and 10% CF_4.In the barrel region, the straws are parallel to the beam axis and are 144 cm long, with their wires divided into two halves, approximately at $\eta = 0$. Charged particles passing through ionize the gas inside the tubes. The resulting voltage difference between the tube and the anode wire in the center causes free electrons to drift towards the wire. Between the tubes, materials with widely varying indices of refraction cause ultra-relativistic charged particles to produce transition radiation and leave much stronger signals in some tubes. With a small average distance between the tubes, the TRT provides large number of tracking points ($\sim$36) per track.

2.2.4 The calorimeters

The calorimeter is situated outside the solenoid magnet which surrounds the inner detector. The calorimeter offers a full coverage in ϕ and up to pseudorapidity $|\eta| < 4.9$. After crossing the tracking system, the neutral and charged particles reach the calorimeter where their energy is deposited, thus energy and direction is

measured. There are two calorimeters optimized to detect different particles : over the η range covered by the inner detector the Electromagnetic(EM) calorimeter is used for identification and energy determination of photons and electrons and the hadronic calorimeter which measures hadronic showers from quarks , gluons and hadronically decaying taus, jets and transverse missing energy measurement. Both of the calorimeters consist of sampling detectors.Sampling detectors are layers of passive, dense material alternated with layers of active material. The passive material causes incident particles to initiate a shower or cascade of secondary particles,which are detected in the active material. Thus after some successive layers the primary particles transfer all their initial energy. Bremsstrahlung and e^+e^- pair production result in electromagnetic showers, their interaction distance is the radiation length X_0 of the material. Nuclear interactions result in hadronic shower, and they develop over large distances. Because of smaller radiation length,the EM calorimeters are located in front of hadronic calorimeters. Since EM showers are denser , the EM calorimeters have finer granularity than the hadronic calorimeter[14, 15]. In the ATLAS calorimeter system, the EM calorimeter covers the region $|\eta| < 3.2$, the hadronic barrel calorimeter HCAL covers the region $|\eta| < 1.7$, the hadronic end-cap calorimeter HEC covers the region $1.5 < |\eta| < 3.2$ and the forward calorimeter FCAL covers the region $3.1 < |\eta| < 4.9$. Over the range $|\eta| < 1.8$ the EM calorimeter is preceded by a presampler detector, used to correct for the energy lost in the material upstream the calorimeter.

2.2.4.1 The Electromagnetic Calorimeter

This is an accordion shaped calorimeter kept in a cold liquid Argon (LAr) vessel. The accordion geometry provides complete ϕ symmetry without azimuthal cracks. The LAr acting as the active material gives finer granularity, easy calibration, radiation

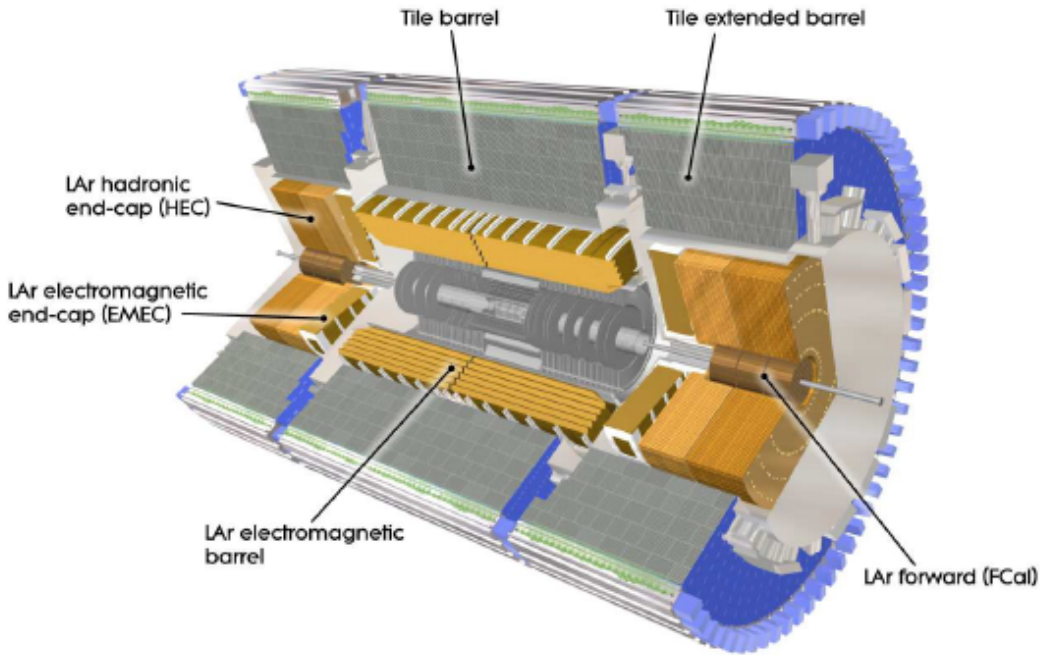

Figure 2.6. Calorimeter[1].

suffering and stabilty. The passive material which are lead absorbers and readout electrodes(Stainless steel and copper) are laid out radially and folded so that particles can not cross the calorimeter without being detected. The detector consists of 4 parts: two half barrels in the region $|\eta| < 1.475$ and two end caps covering a pseudo-rapidity $1.375 < |\eta| < 3.2$. A particle traversing the lead absorber interacts and showers particles which ionize the liquid argon. By applying a bias, electrons in the LAr collect the charge after ionization.The energy of the initial particle is inferred from the amount of ionization.

For precise measurements matched to the Inner detector η coverage in range $|\eta| < 2.5$, the EM calorimeter is segmented into three longitudinal sections with varying granularity which depends on η. The End Cap inner wheel in region $|\eta| > 2.5$ is segmented into two longitudinal sections and has a coarser lateral granularity. A

presampler detector in region $|\eta| < 1.8$ is used to correct for energy losses due to up-stream material. There are a total of 170 thousand readout channels in the EM calorimeter.

2.2.4.2 The Hadronic Calorimeter

The hadronic calorimeter uses two technologies to detect hadrons. The Hadronic End Cap[16] and the TileCal[17]. The hadronic end cap (HEC) is located inside the LAr vessel of EM calorimeter at $1.5 < |\eta| < 3.2$. It consists two independent wheels per end-cap. In the HEC calorimeter copper is used as absorber and LAr as active material. Each of the HEC wheels is build from 32 identical wedge-shaped modules. The Tile Calorimeter (TileCal) surrounds the EM and HEC calorimeter. All Tile calorimeters are divided azimuthally into 64 modules and longitudinally into three layers. The sampling steel-scintillator detector TileCal is divided into a barrel ($|\eta| < 1.0$) and two extended barrels ($0.8 < \eta < 1.7$) .The steel acts as the passive material while the scintillating plastic tiles act as the active material, which emit absorbed energy in form of light. This light is picked by the wavelength shifting fibers and propagated to photomultiplier tube(PMT) where it is detected and amplified.

2.2.4.3 The Forward Calorimeter (FCal)

The FCal covers the pseudo-rapidity range $3.1 < |\eta| < 4.9$. The FCAL calorimeter is integrated into the end-cap cryostat. It is made of three layers: a copper plate absorber for EM detection and two tungsten plate absorber for hadronic particle detection. The copper and the tungsten act as the passive material respectively while the active material in all the three layers is Liquid Argon. Each layer consists of an absorber metal matrix, with longitudinal channels filled with concentric rods and tubes. The rods are at positive voltage, the tubes and the matrix are grounded and

the space in between is filled up with LAr sensitive medium.

The information from calorimeter cells are reconstructed and combined to form discrete objects : towers or clusters. These objects are then input to the jet reconstruction algorithm.

2.2.5 Intermediate Tile Calorimeter

In the Tile Calorimeter , a gap or crack of 680 mm separates the main barrel and the extended barrel. The gap provides space for cryogenic services and cabling. Cables and cooling for the Inner Detector also pass through this gap. The ITC or Intermediate Tile Calorimeter acts as a sub-module in this gap region and helps in improving the calorimeter energy measurement in this gap.. Though it belongs to the extended barrel partition , it is installed after the 64 modules of the extended barrel[18].

Table 2.1. Specifications of ITC

ITC cells	η Region	Thickness	ITC Name	No of Cells
D4	0.8-0.9	311 mm	Plug	1
C10	0.9-1.0	96 mm	Plug	1
E1, E2	1.0-1.2	<10 mm	Gap	2
E3, E4	1.2-1.6	<10 mm	Crack	2

ITC covers the pseudo-rapidity region $0.8 < |\eta| < 1.6$. The structure of ITC depends on the η region where it is located. The geometry is such that the ITC provides the maximum calorimetry and shielding in this region.The η region 0.8-1.0 is called "plug" and consists of a 311 mm thick steel- scintillator stack in η region 0.8-0.9, while a 96 mm steel- scintillator stack in region 0.9-1.0. At η region 1.0-1.6 , due to limited space the ITC consists of scintillator only. The scintillator in the region

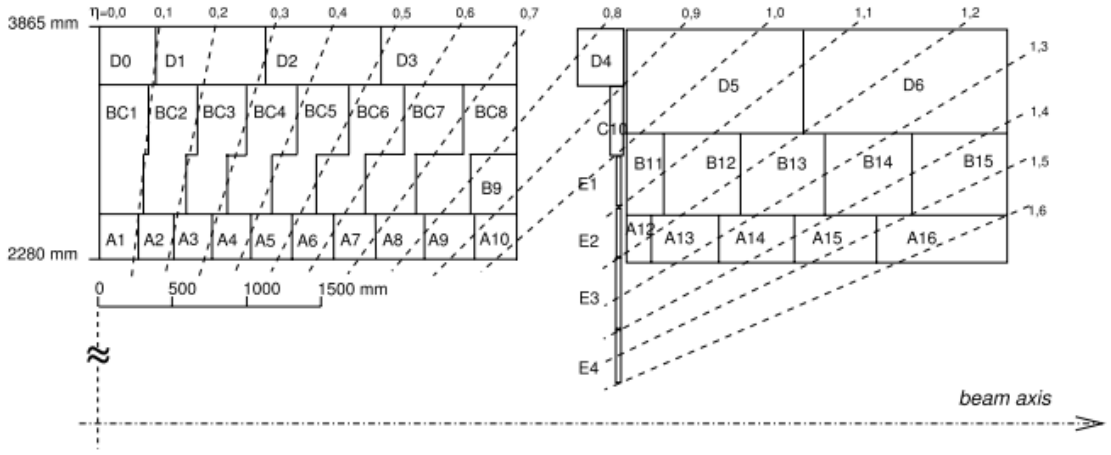

Figure 2.7. The Cells and η of Tile Calorimeter in barrel and extended barrel.

1.0-1.2 is called the "Gap Scintillators" while in region 1.2-1.6 is called the "Crack Scintillators"

2.2.6 MUON Spectrometer

Muons traverse the calorimeters almost undetected, leaving only a very small energy deposition. Muons are measured by large air-core muon spectrometer This reduce the effect of multiple scattering. The muon spectrometer consists of three main parts : toroidial magnetic field to bend muon tracks, the trigger and the momentum measurement chamber[19].

The toroid magnet consists of eight large air-core coil installed symmetrically around the beam axis outside the hadronic calorimeter(barrel toroid) and two end caps. The large barrel toroid covers the region $|\eta| < 1.4$ while the smaller end cap magnets cover the region $1.6 < \eta < 2.7$ and a combination of two acts in the region $1.4 < \eta < 1.6$. In the transition region of $1.0 < |\eta| < 1.4$, precise measurement can not be done because of multiple-scattering. This magnet configuration provides a field that is mostly

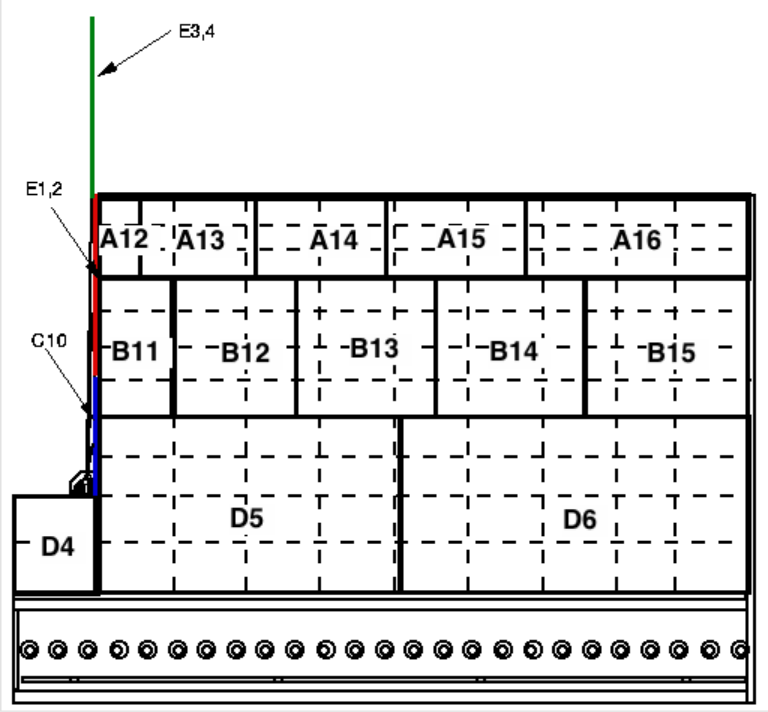

Figure 2.8. Layout of cells in ITC.

orthogonal to the muon trajectories, while minimizing the degradation of resolution due to multiple scattering.

The Trigger consists of Resistive Plate Chambers(RPCs)which covers the barrel region , while the end cap regions are covered by Thin Gap Chambers(TGCs).The triggering system provides bunch-crossing identification (BCID), well-defined p_T thresholds and a measurement of the muon coordinate in the direction orthogonal to the chambers dedicated to precision tracking. Monitored Drift Tubes (MDT) in the barrel region and Cathode Strips Chambers(CSC) in the transition and end-cap regions perform the tracking. MDTs cover the range $|\eta| < 2$ while CSCs with higher granularity operate at high radiation area $2 < \eta < 2.7$. MDT are typical drift tubes of diameter $\sim$ 3cm. These tubes are placed in the Muon Spectrometer forming MDT chambers which consist of three to eight layers of drift tubes.The CSC system consists of two

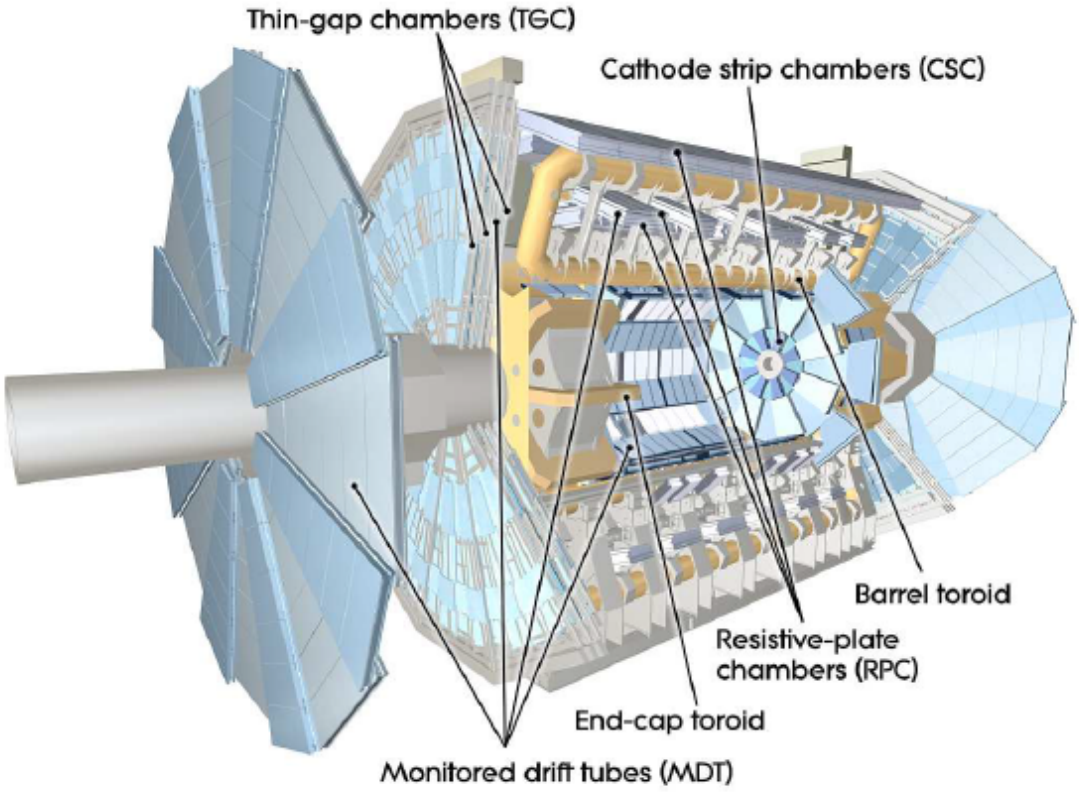

Figure 2.9. Muon Spectrometer[1].

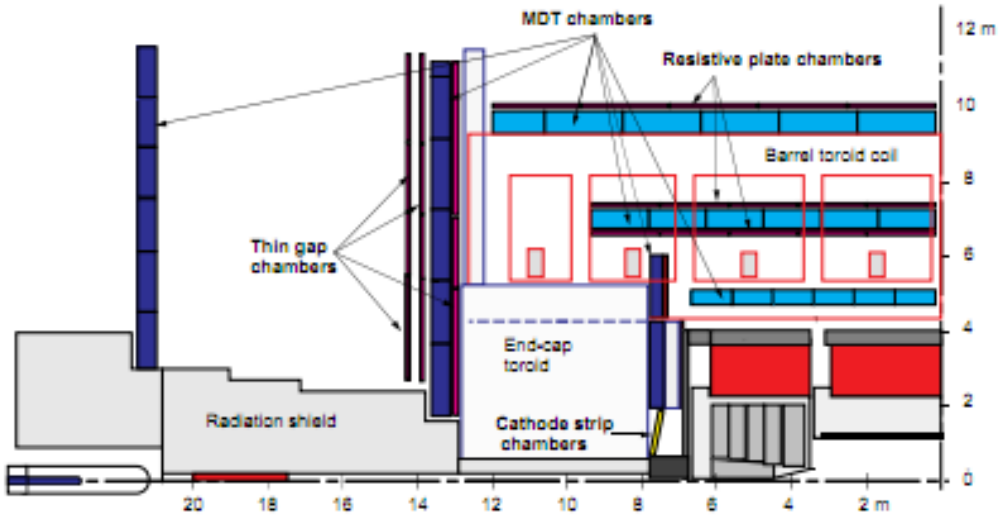

Figure 2.10. Muon spectrometer cross-section.

disks with eight chambers each. MDT are embedded inside two layers of RPC and CSC are embedded in two layers of TGC respectvely.

2.2.7 Trigger System

At the design parameters LHC will operate at a bunch crossing frequency of 40 MHz with 23 interactions occurring per bunch crossing. This may produce one billion events per second. Typically the event size of an ATLAS event is $\sim$ 1.6 MB[20].Most of these events are minimum bias events. Only a fraction of these events are interesting.The trigger system thus developed reduces the rate of events to be stored by a factor of 10^7 i.e. from 40 MHz to 200 Hz.

To achieve this efficient event selection three levels of trigger are used. L1(Level 1), L2(Level 2) and the EF(Event filter). The L2 and EF are together known as the High Level Trigger(HLT). The L1 trigger is implemented using custom-made electronics, while the HLT is based on algorithm level.Figure 2.8 shows the details of the trigger system.

2.2.7.1 LVL1 Trigger

This trigger is responsible for rejecting most of the low energy events. The L1 trigger uses reduced-granularity information from a subset of detectors: the Resistive Plate Chambers (RPC) and Thin-Gap Chambers(TGC) for high-p_T muons, and all the calorimeter sub-systems with the exception of FWD calorimeter for electromagnetic clusters,jets, τ-leptons, total transverse energy and missing transverse energy. The LVL1 trigger decision is based on combinations of objects required in coincidence or veto. Most of the physics requirements of ATLAS can be met, at the LVL1 level, using relatively simple selection criteria[21].

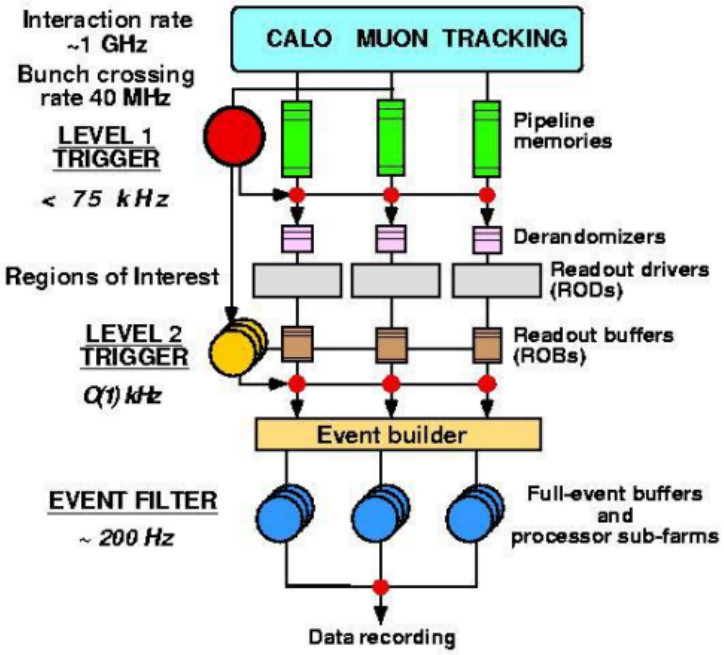

Figure 2.11. Trigger System.

At the LVL1 the event rate is reduced below 75 kHz. The decision time is just 2μsec.Because of such a low processing time, the trigger is hardware based and located closest to the ATLAS detector. LVL1 provides Regions of Interest(RoIs) to the High Level Trigger. LVL1 looks for high p_T electrons and photons, jets, hadronic tau decays, high values of missing transverse energy. In the RoIs the object candidates satisfy certain energy thresholds. Based on multiplicity the RoIs either passes on the information to Level2 trigger or rejects them.

2.2.7.2 LVL2 Trigger

With a *latency* of $40ms$, Level 2 trigger examines RoIs using information from all detectors and sub-detectors.With the information from calorimeters , it reconstructs electrons, photons, muons, jets and calculates the missing transverse energy. From the

RoI data, the LVL2 trigger decides which additional information have to be acquired and moved from the readout buffers (ROBs) to the LVL2 trigger farm. The output rate of this trigger is 2kHz[22].

2.2.7.3 Event Filter

The event filter reduces the event rate from 2kHz to 200 Hz. It first combines the information from different parts of detector , then a final selection is made on the assembled events by same sophisticated algorithms as the reconstruction of the events that are eventually stored. The EF has a latency of 4 s.

The Data Acquisition System(DAQ) controls all data movements. It receives and buffers the event data from the detector-specific readout electronics after a LVL1 trigger accept. The data is then transferred to the LVL2 trigger. In case of a LVL2 accept, all parts of the event data are assembled in the event builder nodes. The full event data are then moved by the DAQ to the EF trigger. In case of an EF accept, the full event data are moved to permanent storage.

2.3 Event Reconstruction

The detector responses from the ATLAS detector are recorded as digitized "hits" and stored in bytestream format(RAW). The process of converting these detector responses into "Physics Objects" like leptons, jets, tracks, vertices, etc is called event construction. Similarly Object Identification is the process of identifying the type of particles from the detector information.

The streamed data is first converted to Raw Data Object(RDO) format, then Physics Objects are reconstructed by algorithms which convert the RDOs into Event Summary Data(ESD). This reduces the size per event to ∼500kB. From ESDs , Analysis

Object Data(AOD) of event size 100kB is derived. ATLAS uses dataset called DPDs. DPDs are made after applying group-wise selection on AODs or ESDs. There are three types of DPDs: D^1PD, D^2PD, D^3PD. D^1PD and D^2PD are small AODs or ESDs. D^3PD is NTUPLE format.

An event must first pass through the trigger system, then the reconstruction algorithm can process the events. The incoming data passes through atleast one set of trigger chains to get a data stream. A data stream contains maximum amount of interesting events. The various Physics data streams are : *egamma*, *muon*, *jet/EtMiss/tau*, *minimum bias*. The minimum bias trigger selects all inelastic interactions.

2.3.1 Electron Identification and Reconstruction

The Electromagnetic Calorimeter is responsible for identifying electrons and photons within a large energy range(5 GeV- 5 TeV) and measuring their energies with a linearity better than 0.5% [23, 24]. High p_T isolated electrons are reconstructed by the *egamma* algorithm. A Sliding window algorithm creates cluster of cells , such that their position corresponds to the maximum amount of energy deposited inside them. The optimal cluster size depends on the particle type being reconstructed and the calorimeter region. Electrons need larger clusters than photons due to their larger interaction probability in the upstream material and as they bend in magnetic field. Several series of these clusters corresponding to different sliding window sizes are build. Based on the Inner Detector tracks, electron and photons are identified. Electrons are pre-selected by the following procedure:

- Start from EM calorimeter clusters with a transverse energy seed of above ~ 3 GeV

- Search for a matching track among all reconstructed inner detector tracks. Tracks are extrapolated to the EM calorimeter, and then required to match the cluster within a coarse $\Delta\eta \times \Delta\phi$ window of 0.05×0.10
- E/p ratio (energy of the cluster over the momentum of the associated track) is required to be below 1.

All electrons must satisfy the above conditions. The energy of the electron is determined by the energy in the cluster while the curvature of the associated tracks defines the charge of the electrons. Based on the requirements , the electrons are classified into three qualities:

- Loose: These electrons are identified based on limited information from the calorimeters. The selection cuts are applied to the measurements in the hadronic calorimeter and the middle layer of the EM calorimeters, and result in rejecting the overwhelming background of hadronic jets. This gives excellent identification efficiency but a very poor background rejection.
- Medium: These have better background rejection. Cuts are applied to energy deposits in the first layer of EM calorimeter and tracking variables. For tracking variables : atleast one hit is found in pixel detector , total number of hits in pixel detector and SCT is greater than nine, and transverse impact parameter satisfies $|d_0| < 5mm$. The medium cuts improve the jet rejection by a factor of 3-4, while the identification efficiency reduces by 10%.
- Tight: These include all particle identification tools. The ratio of transverse energy in a cone of $\Delta R < 0.2$ to the total cluster energy is limited. The track matching to the cluster is more strict. In addition , cuts are applied on the ratio of high-threshold hits to the number of hits in the TRT(rejects background from charged hadrons). Cuts are also applied on the number of vertexing layer hits(rejects secondary electrons).

An isolation selection can be used to further increase the jet rejection. This is done by reducing the rate of non-isolated electron candidate. There are two approaches: calorimeter isolation and tracking isolation. In calorimeter isolation, an additional energy isolation cut is applied to the cluster, using all cell energies within a cone of $\Delta R < 0.2$ around the electron candidate. This cut provides the highest isolated electron identification and the highest rejection against jets. A tracking isolation in the same way limits the high p_T tracks in the inner detector around the electron candidate.

2.3.2 Muon Reconstruction

The ATLAS detector has been designed to provide precision measurements of muons with momenta ranging from approximately 3 GeV to 3 TeV. Muon is identified and reconstructed by information from three of the ATLAS sub-detectors: the muon spectrometer, the Inner Detector and the calorimeter. Based on detector information different types of muon candidates are built[25]. The three different types of muons are :

- Stand-alone Muons: These are reconstructed from tracks in muon spectrometer. To obtain the muon momentum at the interaction point , the momentum from the track is corrected for the parameterized energy loss of the muon in the calorimeter. The energy lost by dE/dX in the calorimeters is estimated using a parametrised method: the expected energy loss is obtained as a function of the amount of material traversed in the calorimeters. The tracks are extrapolated back to the beam line to obtain the angular coordinates ϕ and η. The stand-alone muon reconstruction covers the full muon spectrometer range over $|\eta| < 2.7$. This acceptance cover has a hole around $\eta = 0$ and is degraded in region $1.1 < |\eta| < 1.7$.

Step during reconstruction	Algorithm	
	Staco	Muid
standalone muon reconstruction	MuonBoy	Moore,MuidStandalone
combined muon reconstruction	STACO	MuidCombined
tagged muon reconstruction	MuTag	MuGirl,MuTagIMO

Figure 2.12. Muon Construction Algorithm.

- Combined Muons: These are reconstructed by matching standalone muons to inner detector tracks in the range $|\eta| < 2.5$. This region corresponds to the geometrical acceptance of the inner detector. It improves the momentum resolution for muons with $p_T < 100GeV$. It also suppresses fake muon background arising from pion punch-through or pion and kaon decays in flight. The angular coordinates are provided by the muon trajectory in the inner detector.
- Tagged Muons: Inner detector track is used as a seed for reconstruction of these muons. Reconstruction algorithms then search for track segments in muon chambers that can be associated to inner detector tracks extrapolated to muon spectrometer. The additional tagged muons improve the overall muon construction efficiency. The muon tag reconstruction can identify muons which have been missed by the stand-alone reconstruction.

There are two algorithms to evaluate the muon performance: STACO and MuID[26]. Hence two separate muon collections exist in the AOD file: "StacoMuonCollection" and "MuidMuonCollection". Both the muon combination algorithms create combined tracks. STACO does a statistical combination of the track vectors to obtain the combined track vector. MuId re-fits the combined track, starting from the ID track and then by adding Muon measurements.

The main difference between the two algorithms is the combining of measurements from Inner detector and Muon Spectrometer. The "StacoMuonCollection" merges the two independent measurements from Inner Detector track and Muon Spectrometer track. The "MuidMuonCollection" performs a global fit of all hits associated with tracks in both the detectors.

Muon identification is based on three quality levels. The three different types of muons categorized by the algorithms are regrouped. The three quality levels are :

- Tight Muons: They should be either MuidCombined, or MuidStandalone at $|\eta| > 2.5$
- Medium Muons: Either Tight Muons or MuidStandalone
- Loose Muons: Medium or MuGirl or MuTagIMO are referred as Loose muons.

2.3.3 Jet Construction

At high energy collisions. the presence of partons is overwhelming. Because of color confinement, a highly collimated shower of hadrons is produced. This phenomenon is called hadronization while the shower of particles is called *Jets*. This Jet is detected and reconstructed in the calorimeter using Jet algorithms. Single cells of calorimeter are hard to use, so cells are grouped together into larger objects like *Calorimeter towers* or *Topological Clusters*. These have been discussed in details in chapter 3.

2.3.3.1 Cone Algorithm

The algorithm takes a cone size R_{cone}, a seed threshold T and either a Calorimeter tower or a Topological Cluster of cells as input. The R_{cone} is defined as

$$R_{cone} = \sqrt{\Delta\eta^2 + \Delta\phi^2} \tag{2.3}$$

Two jets with a distance less than R_{cone} will be constructed as one jet. The typical

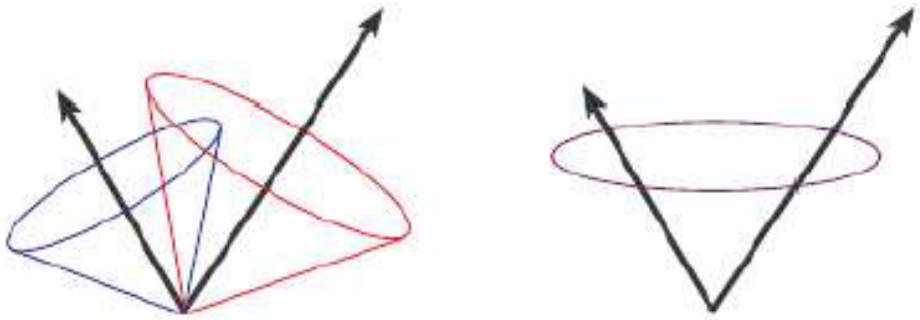

Figure 2.13. Jet Reconstruction with different R_{cone}values.

R_{cone} values are 0.4 and 0.6. Figure 2.13 describes the jet Reconstructed with different values of R_{cone}. The left hand side as two separated cones with a smaller R_{cone}, while the right jet has a higher R_{cone} value.

The towers or topological clusters are arranged in decreasing order of p_T. If the highest p_T object has a p_T greater then the threshold, all the objects with $\Delta R < R_{cone}$ are grouped to a new object. Taking the center of the object a cone is constructed, and all the objects within this cone are grouped to a new object. This is repeated until the direction of cone is stable and the resulting cone becomes the "Jet".

2.3.3.2 H1 Calibration

H1 calibration accounts for the non-compensating response for the hadrons. It applies a weight$w$ to each cell. The weight w is a function of location X_i, energy E_i and volume V_i of the cell. For the electromagnetic showers, the weight factors are about 1 where the signal densities E_i/V_i are high. While for hadronic showers with low signal densities, the weight factors are 1.5.

The jet collection used in this analysis is "AntiKt6Topo". This is reconstructed with anti-k_T algorithm applied to topological cluster. The "6" is the distance parameter R of the algorithm which is 0.6.

The k_T algorithm starts by clustering two particles with the smallest distance d_{ij} and limits at a threshold of d_i. The distances d_{ij} and d_i are defined as

$$d_{ij} = min(k_{Ti}^{2n}, k_{Tj}^{2n}) \frac{(\Delta R)_{ij}^2}{R^2} \quad (2.4)$$

$$d_i = k_{Ti}^{2n} \quad (2.5)$$

where

$$(\Delta R)_{ij}^2 = (y_i - y_j)^2 + (\phi_i - \phi_j)^2 \quad (2.6)$$

where $y_{i,j}$ is the rapidity of the particle. k_T is the transverse momentum of particle, R is the distance parameter. For an $Anti-k_T$ algorithm , n = -1 and for which in the vicinity $\Delta R < R$ of a hard object, all softer objects will be merged with the harder object.If two comparably hard objects are within $R < \Delta R < 2R$ of each other, energy will be assigned to one of them depending upon their relative k_T and distance. For hard objects within $\Delta R < R$ of each other, a single jet will be formed containing both hard objects and the soft objects within their vicinity.

2.3.4 Missing Transverse Energy

The neutrinos having no electric charge and weak interactions do not interact with the detector material and remain undetected. Experimentally neutrinos can be detected as the imbalance of the measured particle momenta in the transverse plane. This imbalance in the overall measured momentum of the hard scattering process is called the missing transverse energy or MET. Although a fraction of MET is faked by measuring inaccuracy of the observable particles, by measuring MET conclusions can be made about neutrinos or other exotic particles which are produced. After measuring and calibrating all the energy deposits in the detector , their sum in the

transverse plane should be balanced out by a vector that corresponds to the transverse momenta of all noninteracting particles that were produced.

$$E_x^{miss} = -\sum_{i=1}^{N_{cell}} E_i Sin\theta_i Cos\phi_i \tag{2.7}$$

$$E_y^{miss} = -\sum_{i=1}^{N_{cell}} E_i Sin\theta_i Sin\phi_i \tag{2.8}$$

The total missing transverse energy is defined as

$$E_T^{miss} = \sqrt{(E_x^{miss})^2 + (E_y^{miss})^2} \tag{2.9}$$

where E_T^{miss} includes contributions from transverse energy deposits in the calorimeters, corrections for energy loss in cryostat and measured muons.

$$E_{x,y}^{miss} = E_{x,y}^{miss,Calo} + E_{x,y}^{miss,Cryo} + E_{x,y}^{miss,Muon} \tag{2.10}$$

Noise contribution is suppressed by limiting the number of cells, N_{cell}. This is done by using cells belonging to topoclusters only. The $E_T^{miss,Calo}$ is defined as summing up all calorimeter cells above a threshold noise. The $E_T^{miss,muon}$ is obtained from the momenta of muons measured in the muon spectrometer over a large range of $|\eta| < 2.7$

$$E_{x,y}^{miss,muon} = -\sum_{rec.muons} E_{x,y} \tag{2.11}$$

The $E_T^{miss,cryo}$ takes into account energy lost in the cryostat between the LAr barrel electromagnetic calorimeter and tile barrel hadronic calorimeter.

The Missing ET thus constructed is referred to as "MET_Final". This missing ET does not depend on the electron and muons. Refined calibration is then used to replace initial calibration cells to achieve higher accuracy. The reconstructed missing ET is called which is denoted as "MET_RefFinal":

$$\begin{aligned} E_{x,y}^{\mathrm{RefFinal}} = \quad & E_{x,y}^{\mathrm{RefEle}} + E_{x,y}^{\mathrm{RefPhoton}} + E_{x,y}^{\mathrm{RefTau}} + E_{x,y}^{\mathrm{RefbJet}} \\ & + E_{x,y}^{\mathrm{RefJet}} + E_{x,y}^{\mathrm{RefSoftJet}} + E_{x,y}^{\mathrm{RefMuo}} + E_{x,y}^{\mathrm{RefCellOut}} \end{aligned} \tag{2.12}$$

Missing ET is described in details Chapter 4.

CHAPTER 3

JETS AND JET CALIBRATIONS

As discussed in Chapter 1, the strong force is mediated by gluons acting upon color charged particles which are quarks, antiquarks and other gluons. For color to be conserved in strong interaction, quarks carry three possible colors, while gluons carry one color and one anticolor. Because of color confinement, quarks and gluons do not appear isolated but exist as color neutral combinations called *hadrons*. Hadrons are of two types: *Baryons* which have three different color and anticolor, and *Mesons* which is a combination of a color and its anticolor.

After a hard scattering at LHC as depicted in Figure 3.1, a recoiling parton fragments and creates a quark-antiquark pair from vacuum. This process produces a shower of quarks and gluons, which then recombine as hadrons. This phenomenon is therefore called *hadronization*. The products of hadronization appear as a spray of collimated particles with the same direction as the initial parton. This spray of hadrons is called the "*Jet*". The high energetic hadrons after entering the detector interact with it. Thus most of the energy is deposited in form of particle showers in the calorimeters. The jets reconstructed from them , can be associated with partonic initial and final state. A schematic representation of Jet Formation is given in Figure 3.2.

3.1 Jet Algorithm

Jets are defined with various jet algorithms. A jet algorithm should be applicable to experimental measurements as well as Monte Carlos. It should be collinear and infrared safe. Collinear safe means, that the splitting of one particle into two collinear

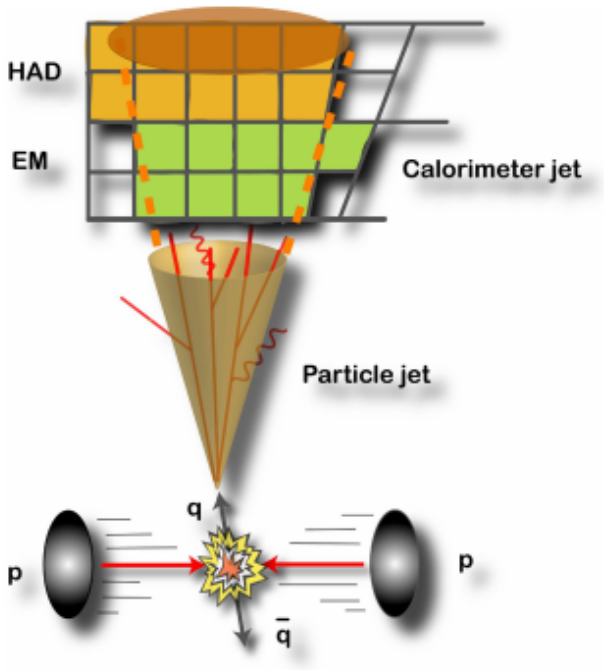

Figure 3.1. The Jet formation.

particles has no effect on the reconstruction. Infrared safe means that the presence of additional soft particles between jet components does not effect the recombination of the particles to the jet.It should also be independent of non-perturbative effects like hadronisation models and underlying event. Many algorithms are used for defining jets. The two most important techniques have been described here: cone algorithms and recursive recombination cluster algorithms.

3.1.1 Cone Algorithms

The term Cone Algorithm is applied to the wide range of jet algorithms which broadly aim to maximise energy (or p_T) in a geometric cone. The algorithm depends on the cone radius R_{cone}, defined in the $\eta - \phi$ plane and a seed threshold T[27].

$$R_{cone} = \sqrt{\Delta\eta^2 + \Delta\phi^2} \tag{3.1}$$

With a more energetic seed , all candidates inside a cone with radius R_{cone} from the seed are summed with it, forming a pseudo-jet. A new cone is again drawn around the pseudo-jet and the procedure is repeated until the configuration is stable. The cone is now considered a jet. The same procedure is repeated for all the seeds. If jets obtained at the end share constituents, they are either split or merged into a single jet depending on the amount of overlap. The seeded cone algorithm is not collinear or infrared safe. This is the reason why cone algorithms are not used any more.

3.1.2 Recursive recombination cluster algorithms

This algorithm is based on pair wise clustering of initial constituents[28]. For each constituent i, two distances are calculated , the distance d_{ij} from other constituents j and distance d_{iB} from the beam axis:

$$d_{ij} = min(k_{Ti}^{2n}, k_{Tj}^{2n})\frac{(\Delta R)_{ij}^2}{R^2} \tag{3.2}$$

$$d_{iB} = k_{Ti}^{2n} \tag{3.3}$$

where R is the algorithm radius parameter.

$$(\Delta R)_{ij}^2 = (y_i - y_j)^2 + (\phi_i - \phi_j)^2 \tag{3.4}$$

and k_T is the transverse momentum. The parameter n governs the relative power of the energy versus geometrical(ΔR_{ij}) scales. Depending on the values of n, three different algorithms are defined. All the three algorithms are collinear and infrared safe.

- K_T algorithm for n = 1[29]. In this algorithm, objects with low k_T are merged first and the final merge is hardest. If the k_T of an object with respect to the beam is lower than its k_T to anything else , it will not be merged any further. Hence soft objects are either merged with hard objects or left alone with low p_T.This algorithm can be used to study the substructure of jets.

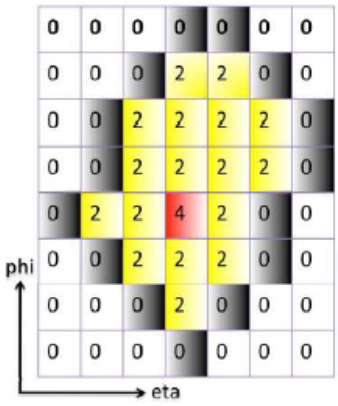

Figure 3.2. Topological Cluster.

- Cambridge/Aachen algorithm for n = 0[30].In this k_T order of the objects is irrelevant and objects near to each other in ΔR are merged first. This information can be again exploited to study the jet substructure, removing small and peripheral subjets to improve the single-jet mass resolution.
- Anti-K_T algorithm for n = -1[31]. Thus in this algorithm, in the vicinity of a hard object ($\Delta R < R$), all softer objects will be merged with the harder object instead of merging with soft particles. Thus the jet boundary is unaffected by soft radiation. This ensures that the anti-k_T algorithm is infrared safe. If two hard objects are within $R < \Delta R < 2R$ of each other, energy is shared. This ensures that anti-k_T algorithm is collinear safe. Jets from this algorithm have very regular cone-like boundaries, and are easy to calibrate.

3.2 Jet Inputs

For a jet algorithm to be executed it needs input seeds to start a cluster. The calorimeter signals from individual cells are taken as inputs. Calorimeter cells are combined to reconstruct the shower structures in the position space.ATLAS provides two different cell cluster algorithms: Calorimeter tower and Topological Clusters.

- Calorimeter Towers: These are constructed by projecting calorimeter cells onto a fixed grid with tower bin size $\Delta\eta\Delta\phi$ = 0.1 x 0.1 in the whole acceptance region of calorimeter with $|\eta| < 4.9$ and $-\pi < \phi < \pi$. Depending on the overlap fraction of the cell area with the towers, each cell contributes the corresponding fraction of its signal to that tower. Tower signal is the sum of possibly weighted cell signals.
- Topological Clusters: In this, shower from each particle entering the calorimeter is represented as three dimensional energy deposit. As shown in Figure 3.3 , they are reconstructed by combinations of cells around seed cells which exceed a threshold signal to noise ratio. The Signal to Noise Ratio $E_{cell}/\sigma_{noise,cell}$should be greater then 4. All neighboring cells of the seed cells are collected in the cluster. Subsequently the neighboring cells should have a threshold of $E_{cell}/\sigma_{noise,cell} > 2$.Finally an additional neighboring cells of threshold $E_{cell}/\sigma_{noise,cell} > 0$ is added to the cluster.

The above two concepts can be combined to get another calorimeter signal object, the *Topological Tower* or *TopoTower*. TopoTowers are build by first creating a topological cluster. A tower is then made by selecting calorimeter cells from topological clusters contained in $\eta \times \phi$ area of 0.1×0.1. Since TopoTowers are made of cells from topological clusters, they are noise suppressed. Figure 3.4 illustrates the three geometric configurations. In the diagram, the calorimeter volume segments represent an area in $\eta \times \phi$, projected outward from the ATLAS interaction point. The blue and orange cells represent the electromagnetic and hadronic calorimeters, respectively.

3.3 Jet Energy Scale

Jet energy scale (JES) corrections aim to calibrate the jet energy measured in the calorimeter to the energy of all the underlying particles that constitute the jet. Al-

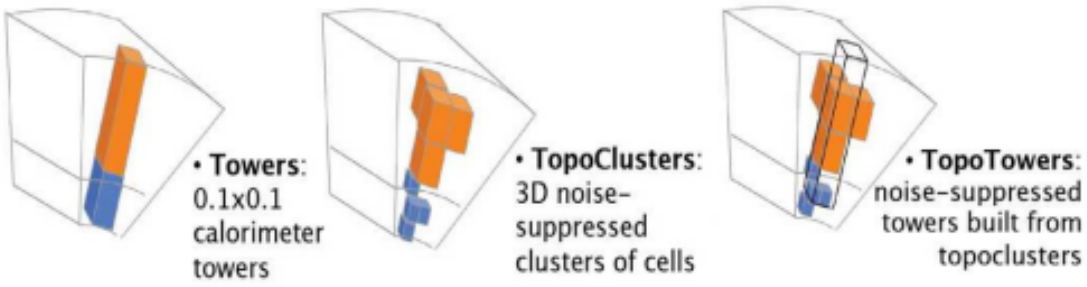

Figure 3.3. ATLAS calorimeter jet input objects.

ternately the Jet energy can be calibrated directly to the energy of the parton but the first approach is preferred. The measured energy can be different from the energy of the initial particle because of many reasons like energy loss in dead material of detector, energy deposited in the detector due to processes other than the hard scattering,detector and electronic noises, jet energy excluded due to size of cluster[32]. The derivation of the jet energy scale calibration and the estimate of its uncertainty are based on a comparison of simulated jets reconstructed from the calorimeter jet constituents with jets built from Monte Carlo.

3.3.1 Jet Calibration

For many physics analysis like the inclusive jet cross section measurement ,the search for Supersymmetric particles or the top quark mass measurement, accurate jet energy measurement is important. Precise jet energy measurement requires the energy calibration from the electromagnetic scale of the constituents to the initial jet energy[33]. Calibration removes the detector designs and clustering effects. ATLAS has developed several calibration methods with different levels of complexity and sensitivity to systematic effects. For all the methods, the reference object is the truth particle jet which is obtained from stable Monte Carlo particles after parton shower and

hadronization. The methods are broadly classified into two categories: the global and the local calibrations.

3.3.2 Global Calibration

In this method, using topo-clusters or topo-towers with energy at electromagnetic scale, the jet algorithm finds the Jets. The single jets are then calibrated with respect to the truth particle jet. There are two methods for global calibration.

- Simple p_T and η-dependent calibration(EM+JES): Jets are reconstructed at the EM scale which is the setting used by default in the calorimeter response. The EMJES calibration corrects the energy and momentum of jets measured in calorimeter, using kinematics of the corresponding Monte Carlo truth jets as reference. The jet energy scale calibration is derived as a global scale function depending on p_T and η. After the calibration of jets with EMJES , the resolution is improved by using other variables as the longitudinal and transverse jet structure. This second step is known as global sequential calibration.
- Global cell energy-density weighting calibration(GCW): In this calibration, jets are first corrected for the different calorimeter response to hadronic and electromagnetic energy depositions in the calorimeters. The correction is obtained in terms of weights applied to the cells belonging to the jets. The weights are different for various calorimeter layers and depend on the cell energy density. The hadronic signal is characterized by low cell energy densities and thus scaled up. The weights are determined by minimizing energy fluctuations between reconstructed and particle jets in Monte Carlo. These weights also compensate for energy losses in dead materials. Jets are found from calibrated clusters or towers, then cells are weighted and a final correction based on p_T and η is applied to ensure that the jet energy is properly reconstructed.

3.3.3 Local Hadron Calibration

In Local Hadron Calibration, topo-clusters are first calibrated to the hadronic scale, then the calibrated topo-clusters are used as input to the jet algorithm. Finally the jets are corrected for residual effects.

Local Cluster weighting calibration.: The properties of clusters are used to calibrate them individually. The weights are determined from Monte Carlo simulations of charged and neutral pions. Jets are found from calibrated clusters and a final correction of the jet energy is applied to account for jet-level effects.

CHAPTER 4

MISSING TRANSVERSE ENERGY

Neutrinos do not deposit any energy in the detector so they remain undetected. But the momentum conservation law allow to calculate the sum of all neutrino momentum in the transverse plane.The colliding protons do not have transverse momentum and hence the sum of transverse momenta of all visible final state particles must be zero. Hence it can be concluded that the sum of transverse momenta of neutrinos is actually the negative of the sum of all visible final state particles.

$$E_T^{visible} + E_T^{invisible} \quad = \quad 0 => E_T^{miss} = -E_T^{visible} \tag{4.1}$$

Study and measurement of E_T^{miss} is vital for many Physics studies at ATLAS[34]. Events with large E_T^{miss} provide us with key signatures for new physics like supersymmetry and extra dimensions. The "Dark Matter" can as well show up as E_T^{miss}. A good E_T^{miss} measurement in terms of linearity and resolution is also important for the reconstruction of the top-quark mass from $t\bar{t}$ events with one top quark decaying semileptonically.

The E_T^{miss} basic quantities are :

- E_x^{miss} : x component of E_T^{miss}
- E_y^{miss} : y component of E_T^{miss}
- $E_T^{miss} = \sqrt{(E_x^{miss})^2 + (E_y^{miss})^2}$
- E_T^{sum} : scaler sum of transverse energies.

4.1 Reconstruction of E_T^{miss}

The E_T^{miss} in ATLAS is constructed from energy deposits in the calorimeter and reconstructed muon tracks.Other E_T^{miss} sources can be underlying events, pile-up, multiple interactions, coherent electronics noise , particles not coming from LHC collisions. The cell based E_T^{miss} algorithm starts from the transverse energy deposited in the calorimeters. It further corrects for energy losses in the cryostat and for the muon energy. Missing Transverse Energy is defined as :

$$E_T^{miss} = \sqrt{(E_x^{miss})^2 + (E_y^{miss})^2} \tag{4.2}$$

where E_T^{miss} components include contributions from transverse energy deposits in calorimeters, cryostat and muon energy loss corrections. Thus the total missing energy is:

$$E_{x,y}^{miss} = E_{x,y}^{miss,Calo} + E_{x,y}^{miss,Cryo} + E_{x,y}^{miss,Muon} \tag{4.3}$$

- $E_{x,y}^{miss,Calo}$: This is obtained from sum over all cells which belong to a cluster:

$$E_{x,y}^{miss,Calo} = -\sum E_{x,y} \tag{4.4}$$

$$E_x^{miss} = -\sum_{i=1}^{N_{cell}} E_i Sin\theta_i Cos\phi_i \tag{4.5}$$

$$E_y^{miss} = -\sum_{i=1}^{N_{cell}} E_i Sin\theta_i Sin\phi_i \tag{4.6}$$

  Two approaches are used to suppress calorimeter noise. In first approach calorimeter cells to be included in E_T^{miss} calculation, should exceed a threshold noise level $|E_{cell}| > 2\sigma_{noise}$[35]. The symmetric cut is important to avoid a bias towards one direction. The second approach consists of using a topological cell clusters which already has a noise cut. In either case, the calorimeter cells are calibrated with H1 calibration. The H1 calibration has already been explained in section 2.3.3.2

- $E_{x,y}^{miss,Cryo}$: In case of calorimeter calibration with GCW, there are sginificant energy losses in hadronic showers in the cryostat between the LAr Electromagnetic calorimeter and Tile hadronic Calorimeter. The E_T^{miss} reconstruction recovers the energy losses in the cryostat using the correlation of energies between last layer of LAr calorimeter and first layer of hadronic calorimeter. The cryostat correction is defined as :

$$E_{x,y}^{miss,cryo} = E_{x,y}^{jet,cryo} \tag{4.7}$$

where all the reconstructed jets are summed in the events and

$$E_x^{jet,cryo} = w^{cryo}\sqrt{E_{EM3}^{jet} \times E_{HAD1}^{jet}}\frac{\cos\phi_{jet}}{\cosh\eta_{jet}} \tag{4.8}$$

$$E_y^{jet,cryo} = w^{cryo}\sqrt{E_{EM3}^{jet} \times E_{HAD1}^{jet}}\frac{\sin\phi_{jet}}{\cosh\eta_{jet}} \tag{4.9}$$

where w^{cryo} is a calibration factor, E_{EM3} is the energy deposits of jet in third layer of EM calorimeter and E_{HAD1} is the energy deposit in first layer of hadronic calorimeter[36]. The w^{cryo} parameter is independent of energy and η.

- $E_{x,y}^{miss,Muon}$ collects the energy of muons. It is calculated from the momenta of muons measured in the range $|\eta| < 2.7$[37].

$$E_{x,y}^{miss,Muon} = \sum_{recomuons} E_{x,y} \tag{4.10}$$

The sum is over all reconstructed muons. In the region $|\eta| < 2.5$, a matched inner detector track is required in order to reduce contributions from fake muons. For higher values of η outside the fiducial volume of inner detector , no matched track is required and muon spectrometer is used. Energy lost by muons in calorimeter is not double counted as it is taken into account in the calorimeter term.

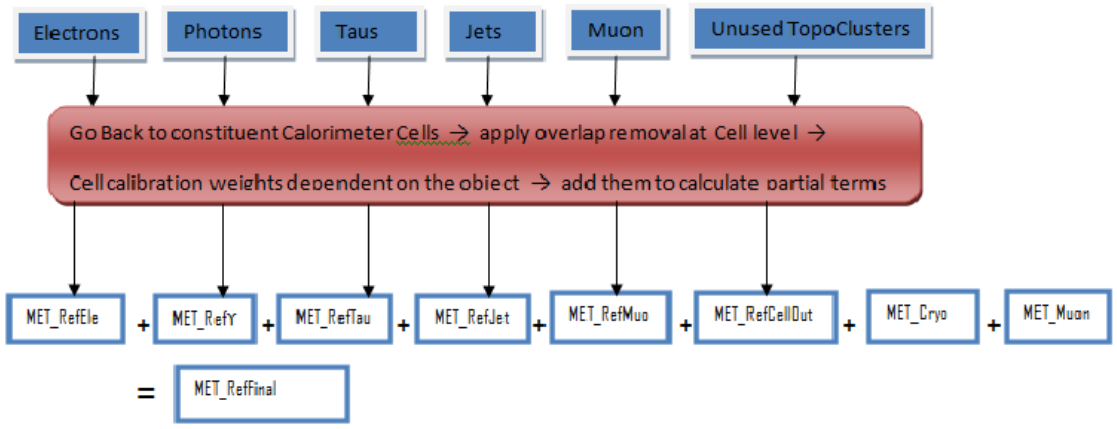

Figure 4.1. Illustration of E_T^{miss} refinement.

4.2 Refined E_T^{miss}

For a more precise calculation of E_T^{miss}, the calorimeter cells are associated with each of the different types of offline reconstructed physics object in chosen order: electrons, photons, muons, hadronically decaying τ-leptons , b-jets, tight jets. Since the calibration of these objects have higher accuracy, the refined calibration of the objects replace the initial global calibration cells. This improves the E_T^{miss} calibration. During association care is taken not to double count cells corresponding to overlapping objects. Cells which are not associated with any objects called *CellOut* are also added during the refined calculation. This calibration of cells is called *refined calibration*. The *CellOut* term contributes mainly for soft physics processes. The total E_T^{miss} is defined as

$$\begin{aligned} E_{x,y}^{RefFinal} = \quad & E_{x,y}^{\text{RefEle}} + E_{x,y}^{\text{RefPhoton}} + E_{x,y}^{\text{RefTau}} + E_{x,y}^{\text{RefbJet}} \\ & + E_{x,y}^{\text{RefJet}} + E_{x,y}^{\text{RefMuon}} + E_{x,y}^{\text{CellOut}} \end{aligned} \tag{4.11}$$

4.3 E_T^{miss} resolution

The E_T^{miss} resolution is calculated as the width variation E_x^{miss} and E_y^{miss} as a function of $\sum E_T$. The E_T^{miss} resolution expressed as $\sigma(E_{x,y}^{miss,True} - E_{x,y}^{miss})$ where $E_{x,y}^{miss,True}$ and $E_{x,y}^{miss}$ are the true and reconstructed E_T^{miss} components. The resolution scales in good approximation as :

$$\sigma(E_{x,y}^{miss,True} - E_{x,y}^{miss}) \quad = \quad a \times \sqrt{\sum E_T} \tag{4.12}$$

where a is the scale factor indicating the resolution quality level. For minimum bias events , resolution contribution comes from two terms : a main fraction from CellOut term, while a small fraction from RefJet term. In minimum bias and jets events $E_{x,y}^{miss,True} = 0$.

4.4 E_T^{miss} linearity

The E_T^{miss} linearity is defined as :

$$Linearity \quad = \quad (E_{x,y}^{miss,True} - E_{x,y}^{miss})/E_{x,y}^{miss,True} \tag{4.13}$$

where E_T^{miss} and $E_T^{miss,true}$ are reconstructed and True E_T^{miss} respectively. For the Linearity, it assumed that $E_T^{miss,true}$ has non zero values and fake E_T^{miss} measurements are small.

4.5 Fake E_T^{miss}

Fake missing transverse energy is the difference between reconstructed and true E_T^{miss}.For an accurate measurement of E_T^{miss}, a good understanding of sources of $E_T^{miss,Fake}$ is needed:

- Fake E_T^{miss} from muons:

Inefficiency while reconstruction of high p_T muon or reconstruction of fake high p_T muon result in $E_T^{miss,Fake}$. Fake muons are due to lower p_T muons or hits from high p_T jet punch-throughs from calorimeter to muon chambers. Although the latter ones strongly contribute to $E_T^{miss,Fake}$, they can be suppressed by cuts on the hits in muon chamber.

- Fake E_T^{miss} from calorimeter:

  $E_T^{miss,Fake}$ in calorimeter is due to hot, noisy or dead calorimeter cells or regions. In the transition regions of calorimeter , there are gaps which result in very poor resolution. Mainly the region $1.3 < |\eta| < 1.6$ gives a huge contribution to $E_T^{miss,Fake}$. As discussed in Section 2.2.5 , the ITC is designed to improve the resolution and performance of the Calorimeter in the transition region $0.8 < |\eta| < 1.6$

- Fake E_T^{miss} from jet leakage:

  The non-instrumented region between the LAr and Tile calorimeter result in jet leakage or fluctuation in large jet energy deposits. This becomes the source of $E_T^{miss,Fake}$. In this region as well the ITC reduces the jet leakage.

- Fake E_T^{miss} from instrumental defects:

  Any hardware problem or instrumental failure can result in $E_T^{miss,Fake}$

- Fake E_T^{miss} from non-collision signals:

  Events like Cosmic muons, beam halo, beam gas which are not the result of LHC collisions also result in $E_T^{miss,Fake}$. These are suppressed through timing and direction requests.

CHAPTER 5

ANALYSIS

5.1 Dataset

The data used in this analysis is taken from the $\sqrt{s} = 7$ TeV runs of the LHC in April 2011.The run numbers: 180448, 180164, 183581, 180241, 180400, 180481, 180122, 180224[38] were used to measure the performance of the Jet Calibration and E_T^{miss} in the central region focussing mainly in the ITC region. For the analysis JetTauEtmiss D3PDs were used from the JETMET group. The datasets belong to period D except for 183581 which is from run period H1. The run number with run periods and the software version for the respective dataset are listed in table 5.1.

Table 5.1. Run Numbers with run periods and version

Run Number	run Period	Version Name	Peak Lumi
180122	D3	f367_m806_p515	$4.35 \times 10^{32} cm^{-2} s^{-1}$
180164	D4	f368_m806_p512	$4.71 \times 10^{32} cm^{-2} s^{-1}$
180224	D5	f368_m806_p621	$4.42 \times 10^{32} cm^{-2} s^{-1}$
180241	D5	f368_m812_p515	$4.42 \times 10^{32} cm^{-2} s^{-1}$
180400	D6	f369_m813_p513	$6.48 \times 10^{32} cm^{-2} s^{-1}$
180448	D6	f369_m812_p515	$6.48 \times 10^{32} cm^{-2} s^{-1}$
180481	D7	f369_m813_p513	$6.57 \times 10^{32} cm^{-2} s^{-1}$
183581	H1	f385_m884_p515	$1.10 \times 10^{33} cm^{-2} s^{-1}$

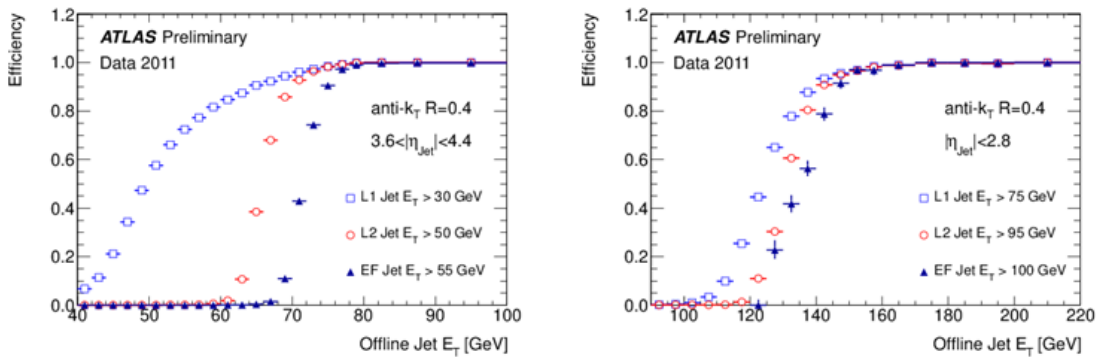

Figure 5.1. Efficiency Curve for L1_J30 and L1_J75 [3].

5.2 Trigger

To select the dijet events, Level 1 triggers (`L1Jx`) : `L1_J10, L1_J15, L1_J30` and `L1_J75` were used. Figure 5.1 shows the trigger efficiency for `L1_J75 and L1_J30` triggers respectively.

Table 5.2 shows the number of events available for each trigger and their respective pre-scales. Since `L1_J75` has a pre-scale of 1 and highest number of events are available for this trigger, `L1_J75` has been used in this analysis. Figure 5.2 shows the p_T distribution of the leading jet for each of the triggers. It can be seen from Figure 5.1 and 5.2 that p_T cut of 120 GeV could keep jets with efficiency more than 30%.

The first step of this analysis is to select good dijet events.

Table 5.2. Trigger with Number of Events

Trigger Name	Total Number of Events :11658900,Events remaining	PreScale
L1_J10	576351	4000
L1_J15	99252	3500
L1_J30	100876	1000
L1_J75	3139542	1

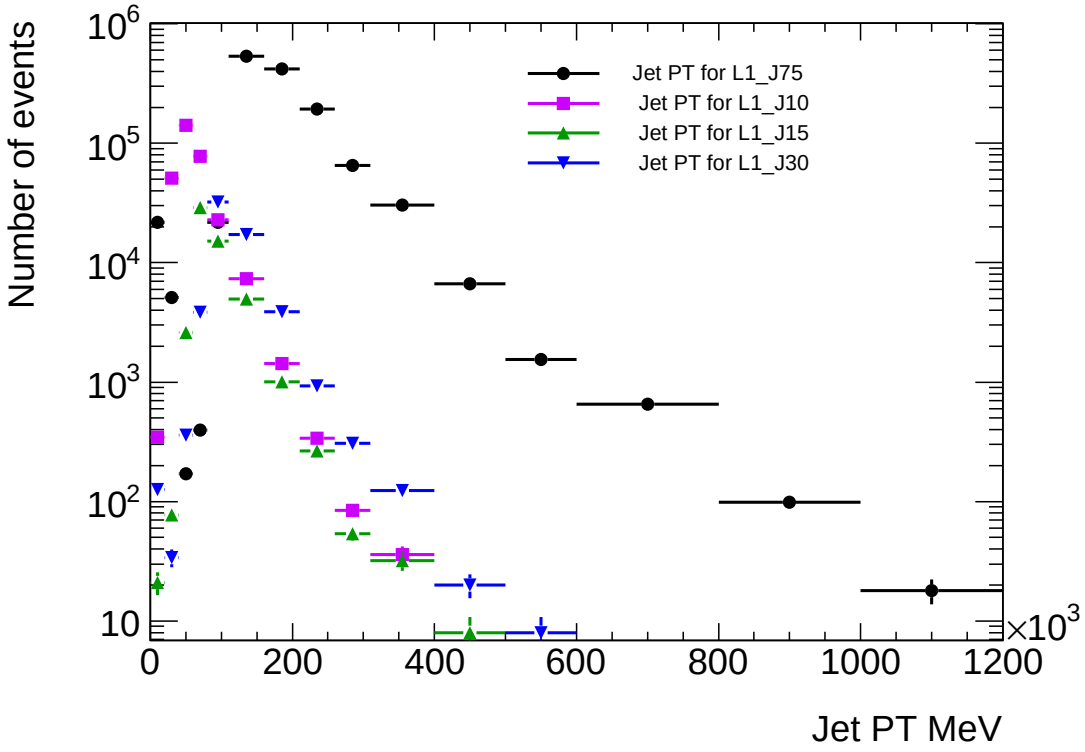

Figure 5.2. Jet p_T distributions for L1_J10, L1_J15, L1_J30 and L1_J75 for jet_AntiKt6Topo.

5.3 Pre Selection of Data

The various primary selections of the events are designed to select good events useful for analysis. These events are selected on the basis of trigger, good runs and events having good primary vertex. They are separated from the dijet events selection so that the current cut efficiency can be estimated. The different pre-selections with their event cut offs have been summarized in table 5.3. The events must pass in order for the pre-selection. The various selection criteria are :

- Trigger Selection: The first selection cut applied to the dataset is of L1_J75 trigger which has been discussed previously. After applying the trigger, percentage of events remaining is 26.93%.

- Good Run List: The GoodRunList or GRL is an xml file which specifies sets of "Good" luminosity blocks over which the data can be run. The data may be "Not GOOD" because of reasons like : noisy cells, sub-detectors switched off, LHC not in stable beam mode, magnets Off. The "Good" events must be present in the GRL. No events were deleted during the GRL selection.
- Primary Vertex selection At high luminosity , many collisions occur at each bunch crossing, so there can be more than one high p_T event in the crossing. The location of the high p_T collision is called the primary vertex. The events are required to have at least one primary vertex that is consistent with the beamspot position and that has at least four tracks associated to it[39].

Table 5.3. Number of events passing the primary selection cuts

Pre Selection Cuts	Number of Events	% Events left
Total Events before any selection	11658900	
Trigger Selection L1_J75	3139542	26.93
Good Run List	3139542	26.93
Primary Vertex Selection	3134400	26.88

5.4 Dijet Event selection

Once the primary selection on the data was made, the Dijet events were selected on the basis of kinematics of the events. To select the dijet events following selection criteria were applied:

- η selection: The leading jet η has been constrained to the region $|\eta| < 2.8$. In ATLAS, the forward regions which are of higher pseudo-rapidity have systematic issues, including lack of coverage of tracking system. Because of this the $|\eta| > 2.8$ region has been excluded from this analysis.

- P_T Selection cut: The leading Jet must have $p_T > 120GeV$ while the second leading jet must have a $p_T > 20GeV$. The 120 GeV cut for the leading jet has been taken as the 30% of the efficiency from the L1_J75 trigger efficiency plot.
- Dijet selection: For selecting a pair of back to back jets, first those events were selected which have more than 1 jet, then events were chosen such that the difference between the azimuthal angles of leading and second leading jet had a $\Delta\phi$ constraint of $170 <= \Delta\phi <= 190$ or $|\Delta\phi| = \pi \pm 0.30$ radians.
- Good Jet selection: Good jets are jets which are neither bad or ugly. "Bad Jets" are jets not associated to in-time real energy deposits in the calorimeters. They arise from various sources, ranging from hardware problems, LHC beam conditions, and cosmic-ray showers. While "Ugly Jets" correspond to real energy depositions in region where the energy measurement is not accurate,like the transition region between barrel and end-cap and problematic calorimeter regions. The Jet cleaning cuts reject electron, photons or muons[40]. For the selection jet_AntiKt6Topo_isUgly and jet_AntiKt6Topo_isBadMedium leading and second leading jets were filtered out.

Table 5.4 shows the different cuts applied to select dijet events along with number of events after each cut and the corresponding cut efficiencies. After the dijet event

Table 5.4. Number of events after Dijet event selection

Dijet Selection Criteria	Number of events left	%events left from total # of events
η selection cut	3053339	26.19
p_T selection cut	2852165	24.46
Back to Back Jets	1502750	12.89
Good Jet Selection	1489128	12.77

selection, the various distribution plots were drawn for the leading and second leading

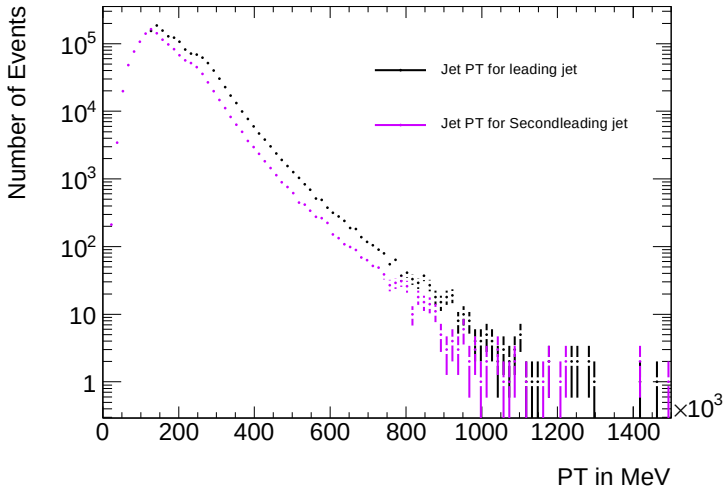

Figure 5.3. Leading and second leading Jet p_T compared.

jets. Figure 5.3 shows the comparison of the p_T of two leading jets. As it can be seen in the figure that the p_T of leading jets starts from 120 Gev while the p_T of second leading jet starts from 20 GeV. This satisfies the p_T selection which we have applied.

Figure 5.4a illustrates the η distribution of the two leading jets. From the figure it can be seen that leading jet plot shows the trigger inefficiencies at $|\eta| \sim 0$, 1 and 1.6. While distribution of second leading jet η is smoother. This is because of the fact that Jet1 or the leading jet is used for triggering and is biased by the detector efficiency while J2 or second leading jet is unbiased. Figure 5.4b illustrates the ϕ distribution of the two leading jets. As expected the distribution is uniform across the ϕ for both the jets.

Figure 5.5 (a,b) describe the η distribution versus jet p_T distribution of the leading and second leading jets respectively. η of Jet1 is within 2.8 while Jet2 covers the whole η range. From the distribution it is evident that high p_T Jet1 and Jet2 are more central. Figure 5.6 (a,b) shows the distribution of E_T^{miss} versus Jet1 and Jet2 p_T

respectively. `MET_RefFinal_et` variable is taken as the Final MET. From the plots it can be seen that events with high E_T^{miss} decreases for high p_T jets and there is dominance of events with lower E_T^{miss} for higher p_T.

5.5 Selection of "Central" and "Free" Jet

As discussed previously, there is a bias because of the trigger decision on the first two leading jets. To remove this biasing the "Tag and Probe" method is applied and one jet is choosen as the "Tag" jet in the central region, while the opposing jet becomes the "Probe" jet.

5.5.1 Tag and Probe Method

After all the primary selections the leading and second leading jet are categorized into the "Central" and "Free" jets The central jet is constrained within the central region $0.1 <= |\eta| <= 0.5$, while the free jet remains free anywhere in the region $|\eta| <= 2.8$. To select the central and free jets the following steps are done:

- The $|\eta|$ of the two highest p_T jet is checked. The jet with $0.1 <= |\eta| <= 0.5$ becomes the *Central Jet* while the other jet becomes the *Free Jet*.
- If both the jets lie in the given region of $|\eta|$, one of the jets is randomly picked up as the *Central Jet* while the other becomes the *Free Jet*.

The figures 5.7-5.9 show the p_T, η, ϕ distributions of Central and Free Jet. As it can be seen from the figures, there is no bias in the jets after applying selection of central and free jets. The p_T distribution for both the Central and Free Jets overlap each other. From the η distribution , its is clear that the Central Jet is limited in the region $0.1 < |\eta| < 0.5$, while the Free jet can be anywhere in the region such that $|\eta| \leq 2.8$

5.6 Analysis of E_T^{miss} and Jet Calibration

For the analysis of Missing E_T and jet calibration , the dataset was divided into three different p_T regions. The dataset was divided based on the p_T of the Central jet. This hepled in understanding the E_T^{miss} and jet calibration in an easier way.

- $120GeV \leq$Central Jet$p_T \leq 200GeV$
- $200GeV \leq$Central Jet$p_T \leq 280GeV$
- $280GeV \leq$Central Jet$p_T \leq 360GeV$

The η dependence of the different quantities were observed as a function of the free jet η as the central jet was constrained in a very small central η region.

5.6.1 Study of E_T^{miss} performance

This section describes the studies of $E_T^{miss}(RefFinal)$ in dijet events. The performance of E_T^{miss} with respect to Jet η is studied to get an overview of behavior of E_T^{miss} across the calorimeter, specially the ITC region which is $0.8 < |\eta| < 1.6$. Also the resolution and scale of E_T^{miss} with respect to $E_T^{miss}(RefJet)$ is studied to get an overview of the performance of *RefFinal* E_T^{miss}.

Figure 5.10 illustrates the distribution of `MET_RefFinal_et` for the three different p_T regions. The E_T^{miss} has been plotted for the three p_T regions after normalizing to unit area. For a p_T range $280GeV \leq p_T \leq 360GeV$, there is more fraction of events with higher E_T^{miss} then the other two p_T regions.

Figure 5.12-5.15 show the distributions of E_x^{miss} and E_y^{miss} mean and resolution with respect to Free Jet η. For drawing the distribution, the Central Jet is divided into three p_T regions. Each p_T regions are taken separately and divided into bins of η of 0.2. For each bin of η, E_x^{miss} and E_y^{miss} are plotted. The distributions of E_x^{miss} and E_y^{miss} for each η bin look like Gaussian distribution. For all the η bins, the histograms are fitted with the Gaussian. The Gaussian mean and statistical mean of E_x^{miss} and E_y^{miss} are plotted for each η bin in the three different p_T regions. Figure 5.11 show the Gaussian fit of E_x^{miss} for the first p_T region. The Gaussian and statistical mean overlap each other, indicating that the distributions are indeed Gaussian. The other Gaussian fits of E_x^{miss} and E_y^{miss} have been included in Appendix A.

The resolution of the two E_T^{miss} components is directly measured from reconstructed quantities, assuming the true values of E_x^{miss} and E_y^{miss} are zero. The resolution is estimated from the width of the E_T^{miss} components in bins of Jet η.

From figure 5.12, there is increase in fluctuations of mean ET_x for higher Jet p_T. It moves from the $+veE_x^{miss}$ to $-veE_x^{miss}$ values. The resolution of E_x^{miss} improves for lower Jet p_T as in Figure 5.13. Also the resolution is worst in the ITC region which is $0.8 < |\eta| < 1.6$.

Unlike E_x^{miss}, E_y^{miss} is always less than 0 throughout all p_T ranges as can be seen in figure 5.14, though at higher p_T there are more fluctuations. The resolution of E_y^{miss} deteriorates as well with Jet p_T and also in the ITC region as shown in figure 5.15.

An evaluation of the E_T^{miss} performance has been obtained by studying the E_T^{miss} components resolutions as a function of the total transverse energy $\sum E_T$ also.

$$\Sigma E_T \quad = \quad \Sigma_{i=1}^{N_{cell}} E_i \sin\theta_i \tag{5.1}$$

where E_i and θ_i are energy and polar angle respectively of topocluster cells. The resolution in this case is estimated as the $E_{x,y}^{miss}$ distribution in bins of $\Sigma E_T(RefJet)$. Figure 5.16 and 5.17 show the mean while Figure 5.18-5.19 show the resolution of E_x^{miss} and E_y^{miss} as a function of $\Sigma E_T(RefJet)$. In figure 5.20 and 5.21, the E_T^{miss} is scaled event-by event by the ratio of $\frac{\Sigma E_T(RefJet)}{\Sigma E_T}$ that is $\frac{\text{MET\_RefJet\_sumet}}{\text{MET\_RefFinal\_sumet}}$ plotted as a function of $\Sigma E_T(RefJet)$, `MET_RefFinal_sumet`.

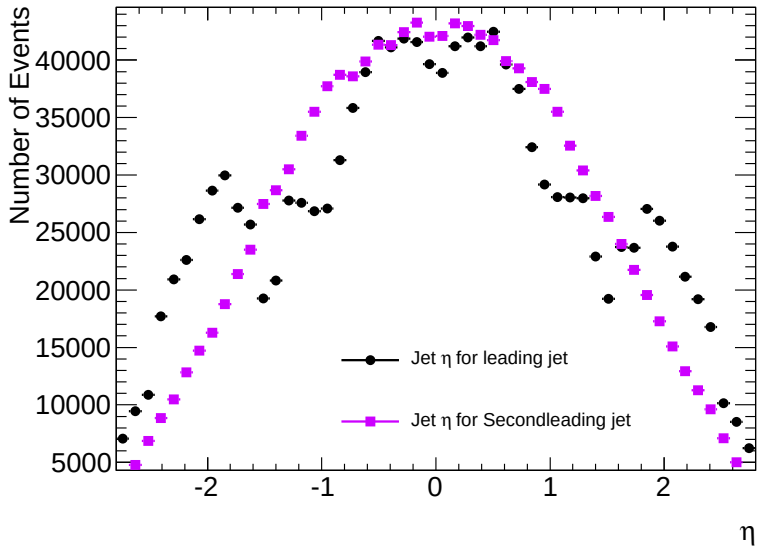

(a)

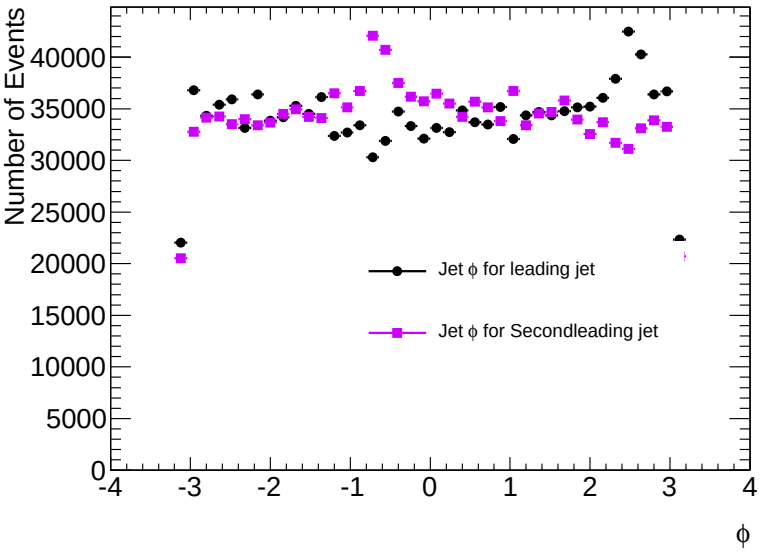

(b)

Figure 5.4. (a)η of leading jets (b)ϕ of leading jets.

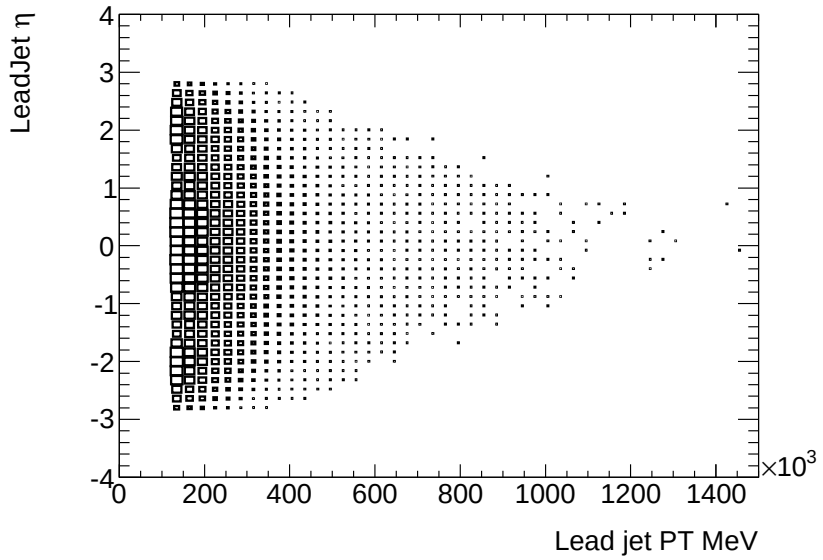

(a)

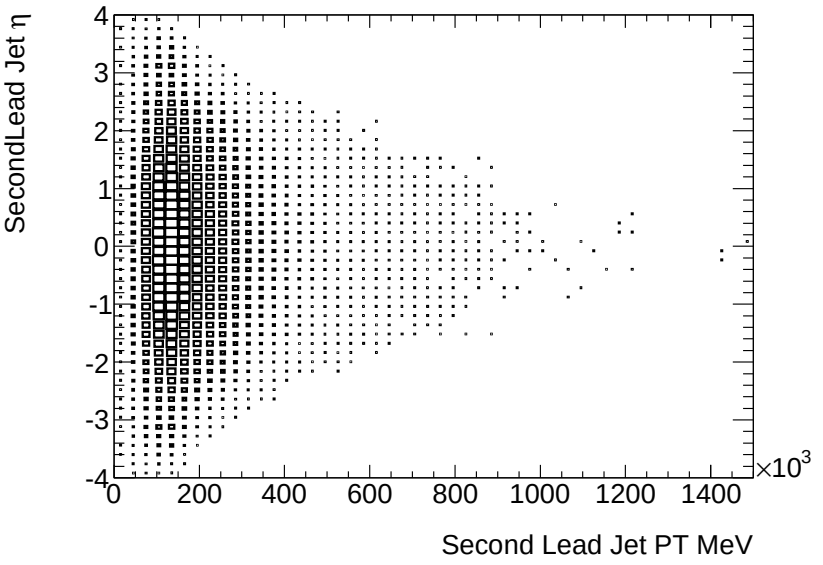

(b)

Figure 5.5. (a)η v/s Leading Jet p_T (b)η v/s second leading jet p_T.

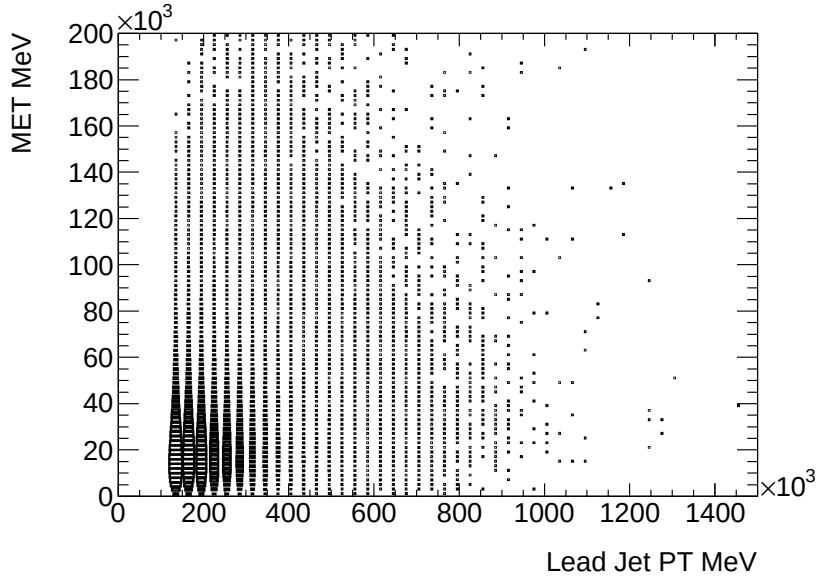

(a)

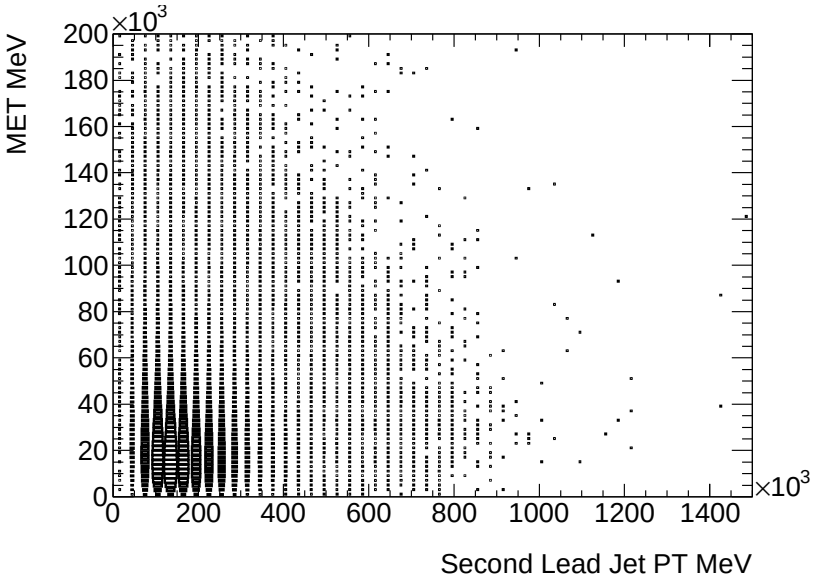

(b)

Figure 5.6. (a)MET v/s leading jet p_T (b)MET v/s second leading jet p_T.

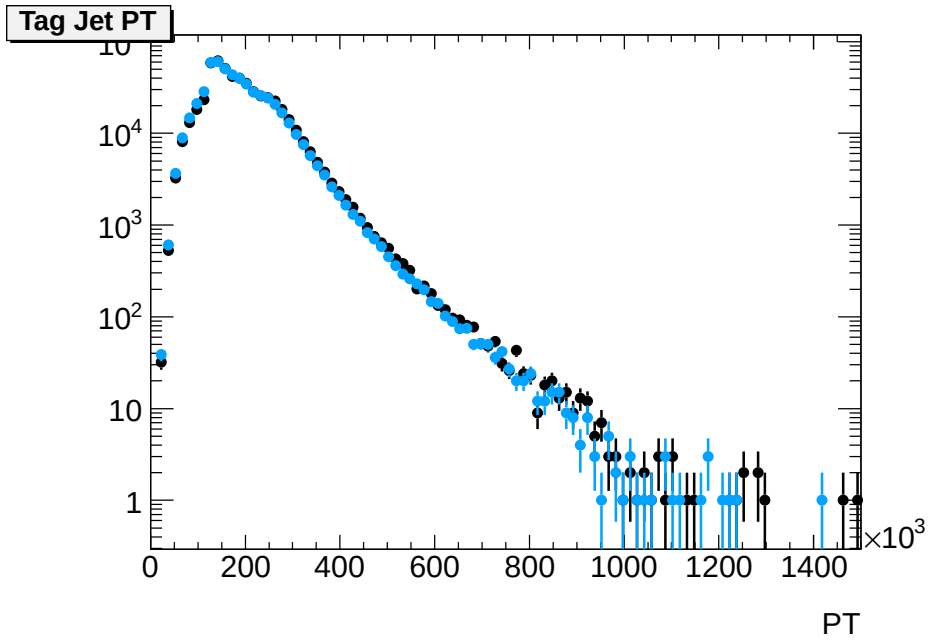

Figure 5.7. p_T distribution of Central and Free Jet.

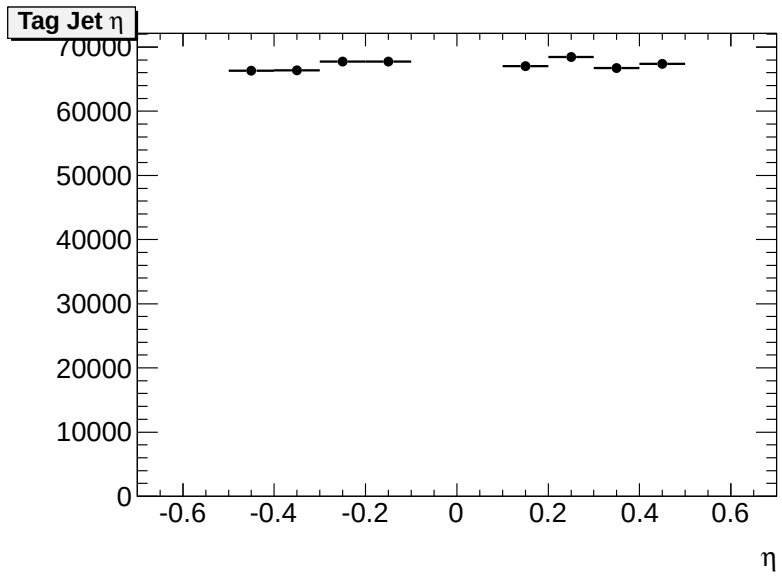

(a)

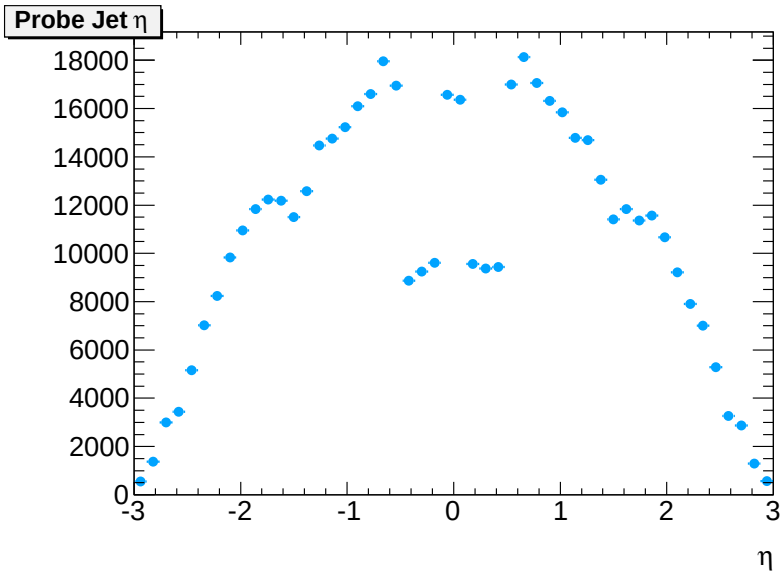

(b)

Figure 5.8. (a)Central Jet η (b)Free Jet η.

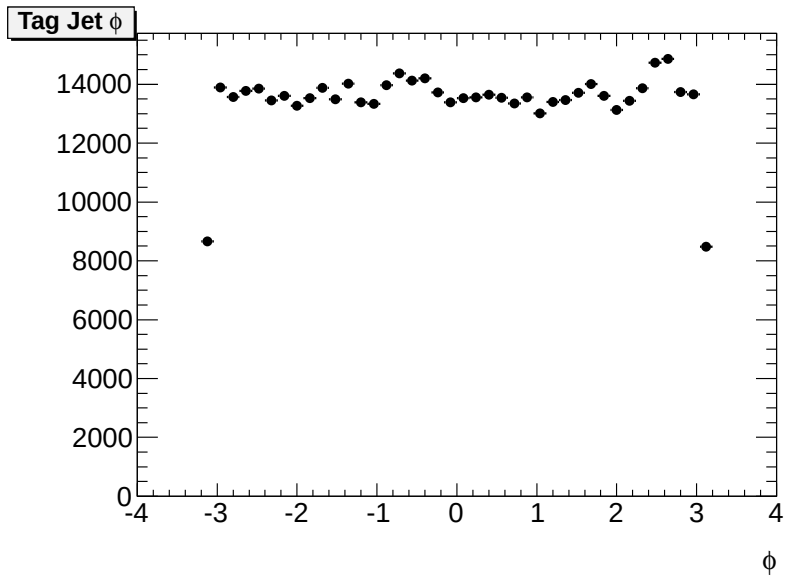

(a)

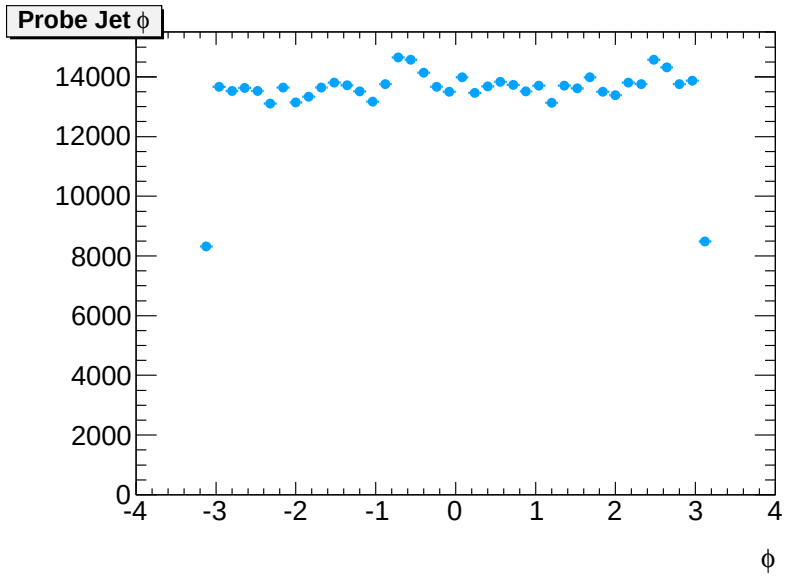

(b)

Figure 5.9. (a)Central Jet ϕ (b)Free Jet ϕ.

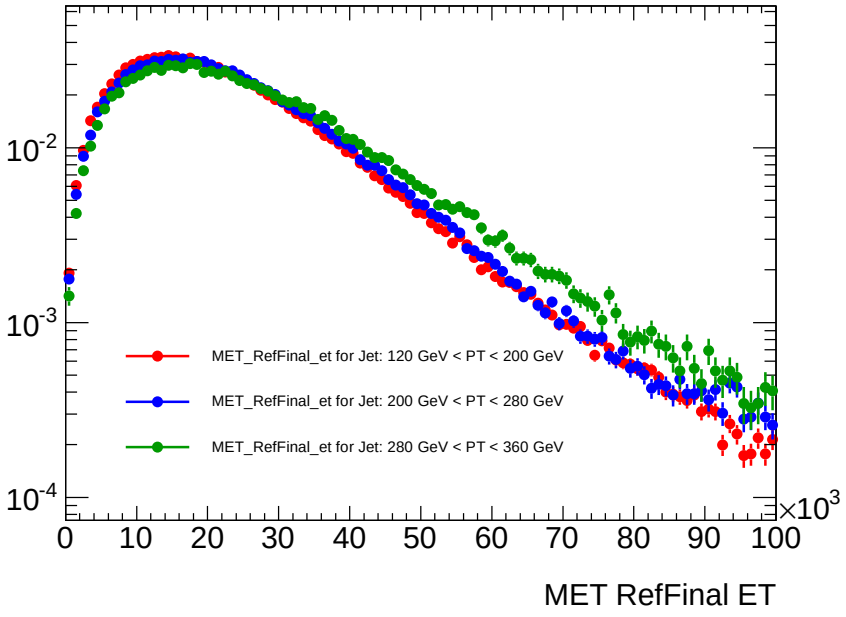

Figure 5.10. E_T^{miss} for the 3 p_T regions.

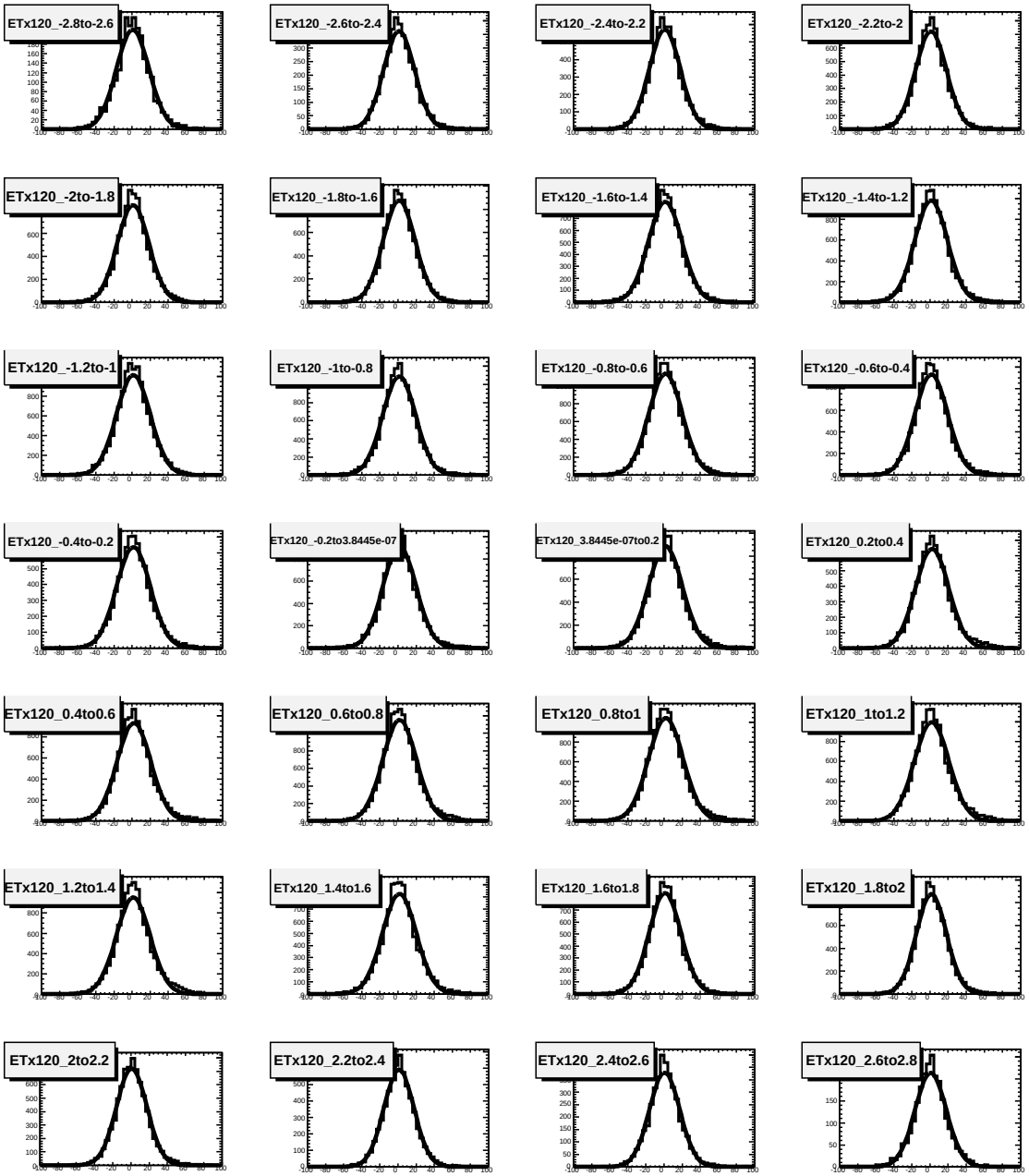

Figure 5.11. Gaussian Fit of E_x^{miss} at each η bin for Central Jet p_T in range $120GeV \leq p_T \leq 200GeV$.

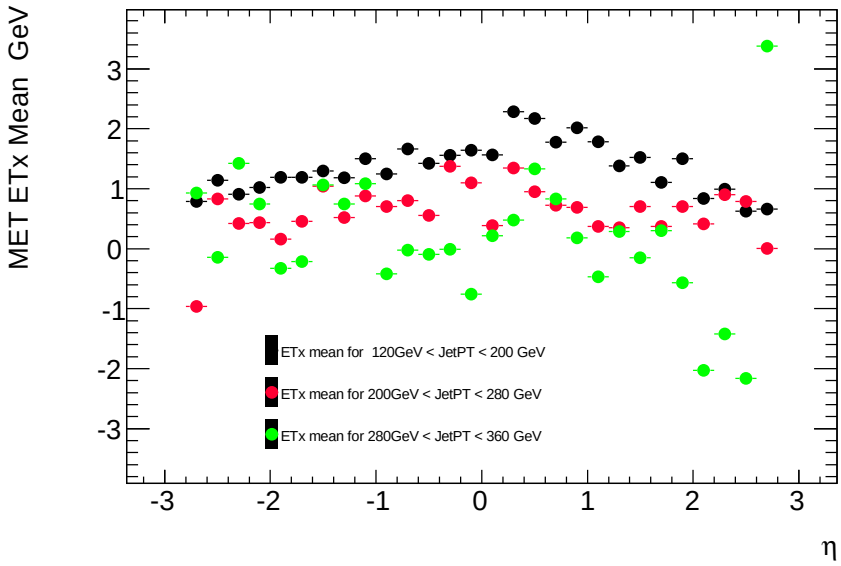

Figure 5.12. E_x^{miss} mean.

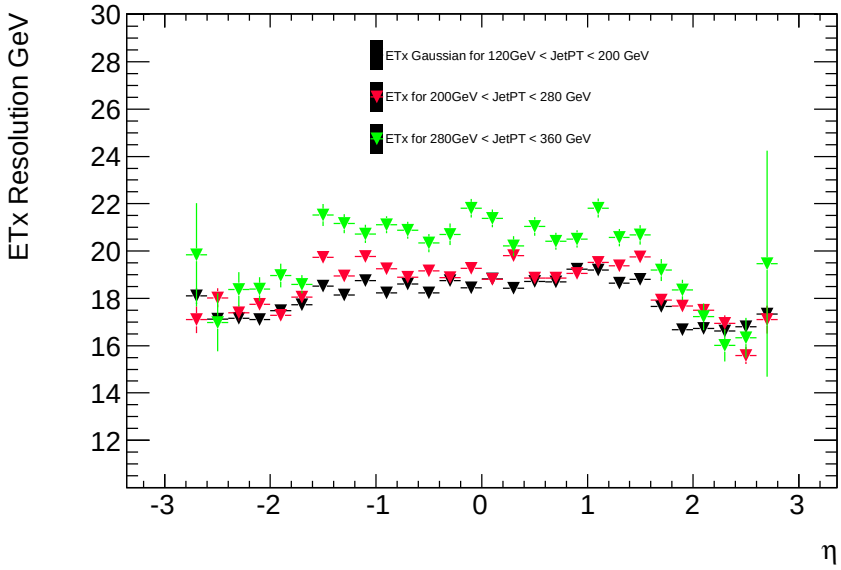

Figure 5.13. E_x^{miss} resolution.

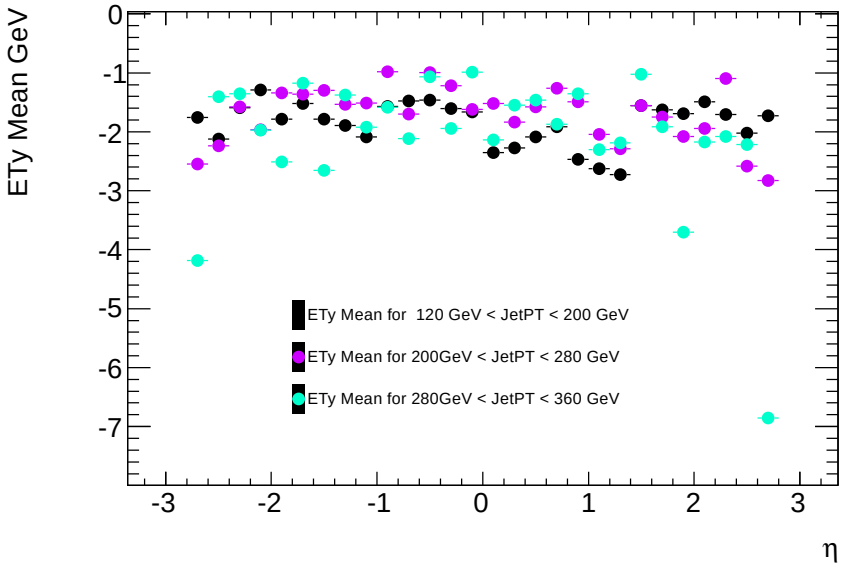

Figure 5.14. E_y^{miss} mean.

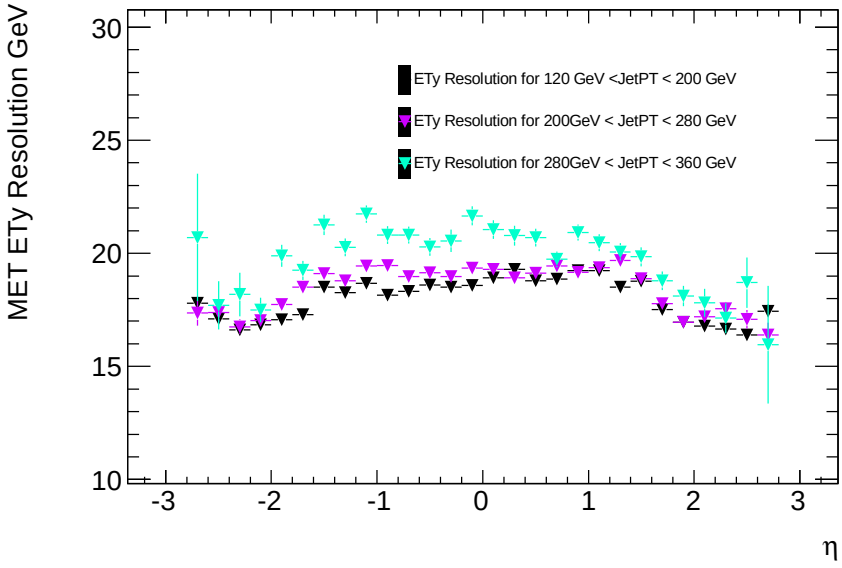

Figure 5.15. E_y^{miss} resolution.

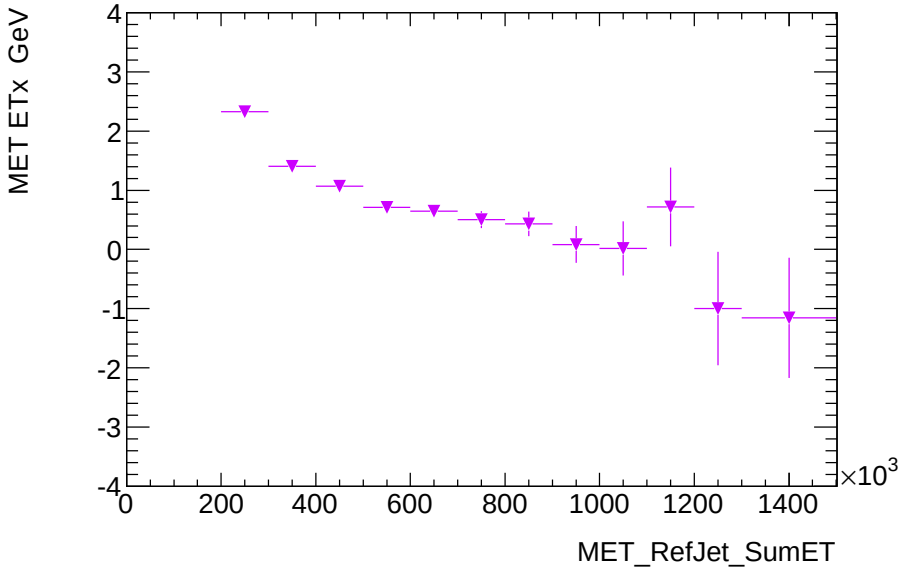

Figure 5.16. E_x^{miss} mean in bins of $\Sigma E_T(Jet)$.

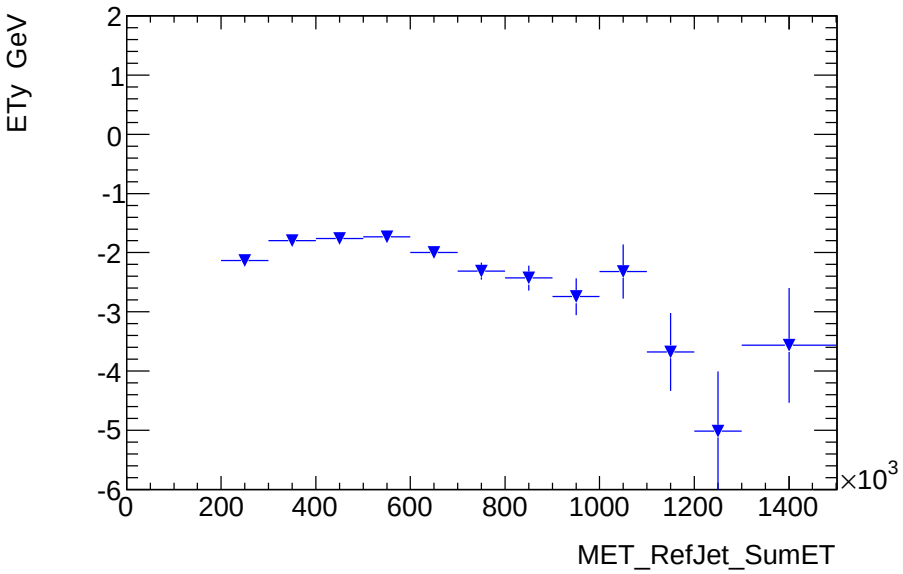

Figure 5.17. E_y^{miss} mean in bins of $\Sigma E_T(Jet)$.

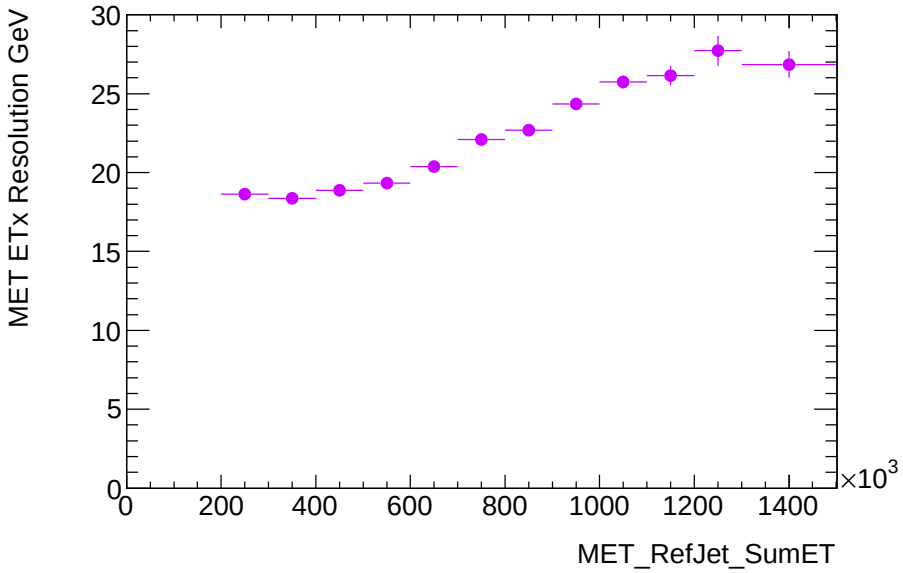

Figure 5.18. E_x^{miss} resolution in bins of $\Sigma E_T(Jet)$.

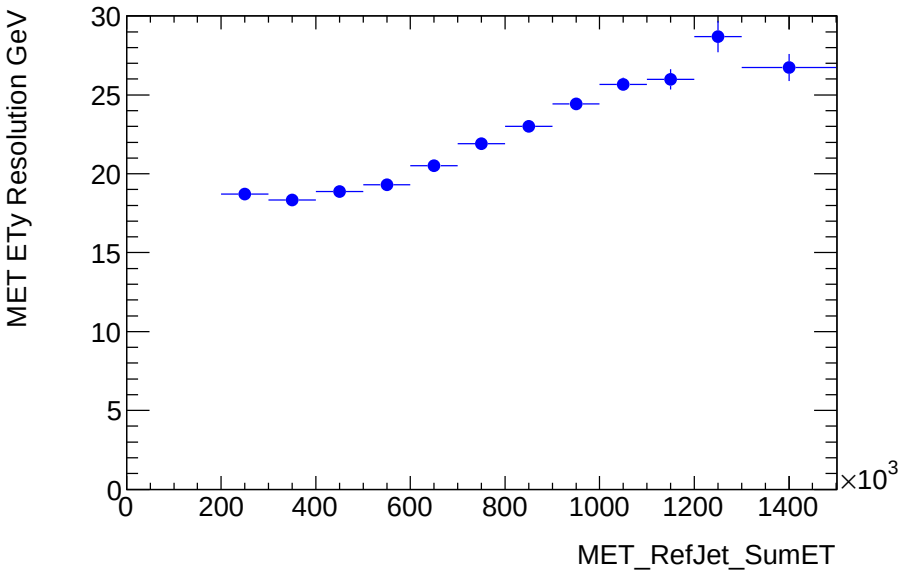

Figure 5.19. E_y^{miss} resolution in bins of $\Sigma E_T(Jet)$.

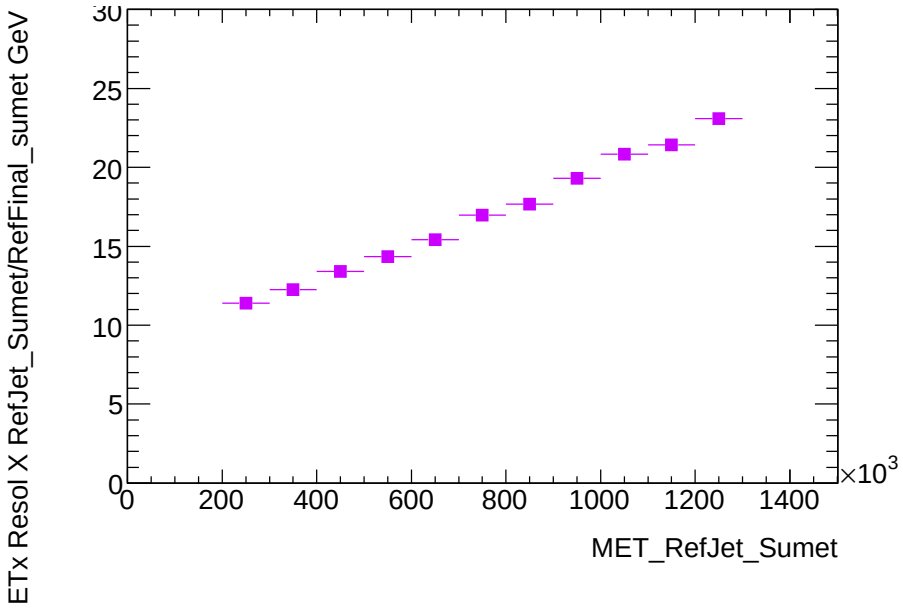

Figure 5.20. E_x^{miss} resolution scaled by $\frac{MET\_RefJet\_sumet}{MET\_RefFinal\_sumet}$ in bins of $\Sigma E_T(Jet)$.

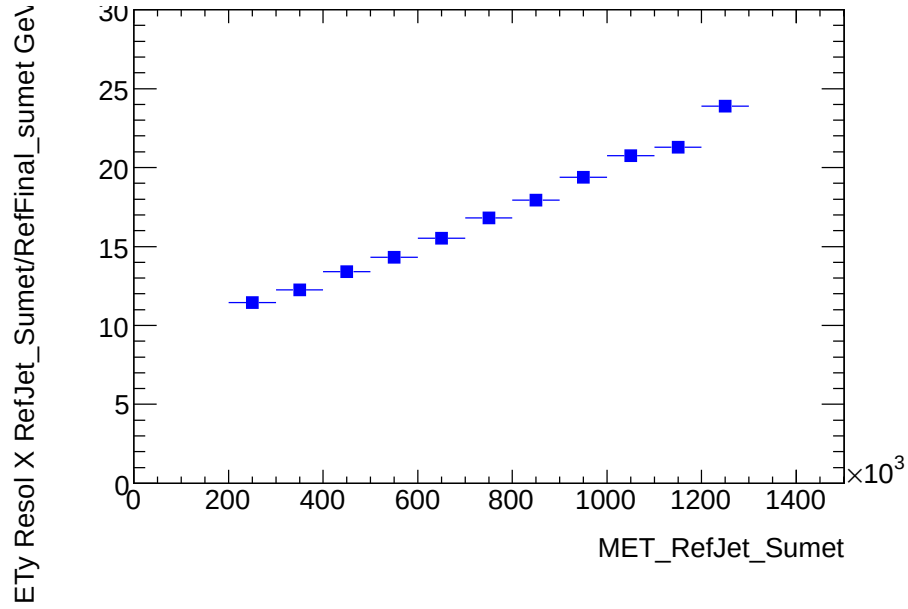

Figure 5.21. E_y^{miss} resolution scaled by $\frac{MET\_RefJet\_sumet}{MET\_RefFinal\_sumet}$ in bins of $\Sigma E_T(Jet)$.

5.6.2 Jet corrections and Calibration

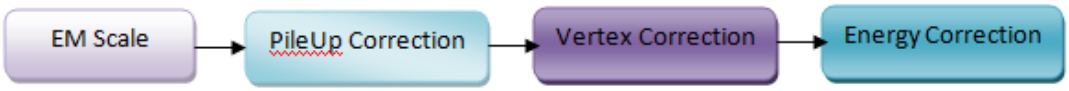

Figure 5.22. Steps of EMJES calibration.

As discussed in section 3.3, `EMJES` calibration technique is employed for Jet Energy Scale Calibration[41]. The various steps of EMJES is illustrated in Figure 5.22. The first step is the electromagnetic scale correction. Then a correction is applied which accounts for energy contribution from pileup. This correction is applied from minimum bias data as a function of number of reconstructed vertices and the jet η. A correction is then done to adjust the momentum of the jet such that the momentum unit vector points from the leading vertex. The final correction restores the reconstructed jet energy to the energy of the reference jet in the Monte Carlo simulations. As discussed in section 3.3, most of the jet calibration is determined by the jets from Monte Carlo. Since Monte Carlo can never be exactly correct, so in this analysis, the calibration using real data is verified.

For a $Anti - K_T$ topo Jet of radius 0.6, the calibrated and uncalibrated Jet can be expressed as

$$\texttt{jet\_AntiKt6Topo\_pt} = \texttt{jet\_AntiKt6Topo\_emscale\_pt} \times \texttt{jet\_AntiKt6Topo\_EMJES}$$

where `jet_AntiKt6Topo_pt` is the calibrated jet while `jet_AntiKt6Topo_emscale_pt` is the uncalibrated Jet at EM scale.To confirm the above mentioned equation , the distribution of $\frac{jet\_AntiKt6Topo\_pt}{jet\_AntiKt6Topo\_emscale\_pt}$ is compared with distribution `jet_AntiKt6Topo_EMJES` which is the correction factor as a function of η. As seen in Figure 5.23 , both the

distributions approximately overlap each other confirming the above equation. The

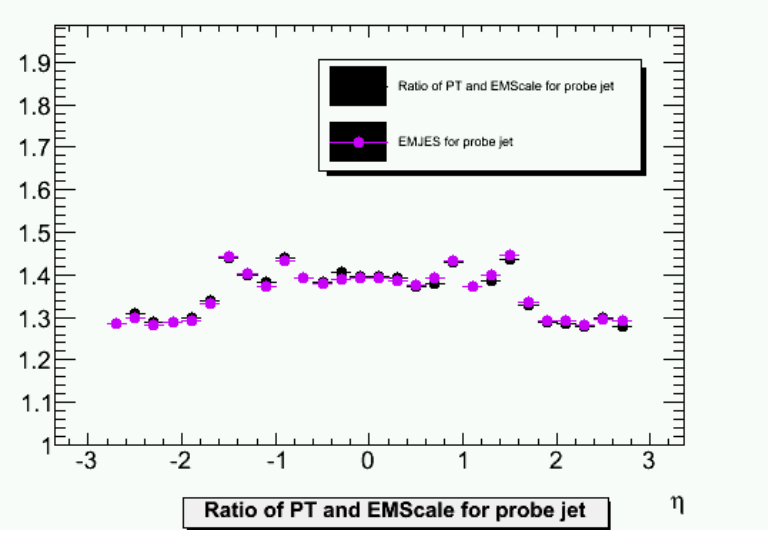

Figure 5.23. Distribution of $\frac{jet\_AntiKt6Topo\_pt}{jet\_AntiKt6Topo\_emscale\_pt}$ and $jet\_AntiKt6Topo\_EMJES$.

next step is to calculate the Asymmetry between the central jet and the free jet. The Asymmetry is defined by the following equation:

$$A = \frac{p_T^{Central} - p_T^{Free}}{p_T^{avg}} \tag{5.2}$$

The calculation of the Asymmetry and the resolutions give a better understanding of the jet energy scale corrections. For this purpose the Asymmetries are calculated for both the calibrated and uncalibrated jets.

$$\frac{\text{jet\_AntiKt6Topo\_pt} - \text{jet\_AntiKt6Topo\_emscale\_pt}}{\text{jet\_AntiKt6Topo\_pt}} = 1 - \frac{1}{\text{jet\_AntiKt6Topo\_EMJES}} \tag{5.3}$$

The correction factor as given by $1 - \frac{1}{\text{jet\_AntiKt6Topo\_EMJES}}$ is also plotted on the same scale. These distributions give an understanding of the calibrations applied on the Jets, specially for the ITC region. The ITC region has two sets of calibrations: first calibration done by EMJES, the other calibration done by the ITC group at UTA.

For plotting the Asymmetry distribution ,the central jet is divided in three p_T regions. For $120GeV \leq p_T \leq 200GeV$ the region is divided into bins of η of 0.1 because of large statistics, while for $200GeV \leq p_T \leq 280GeV$ and $280GeV \leq p_T \leq 360GeV$ the regions are separately divided into η of 0.2. For each bin of η, the Asymmetry of Calibrated Jet and Asymmetry of Uncalibrated Jet are plotted. The correction factor $1 - \frac{1}{\text{jet\_AntiKt6Topo\_EMJES}}$ is plotted on the same scale. As the distributions seem to be Gaussian, each of the correction distributions:$A_{Calibrated}$,$A_{EMSCALE}$ and $1 - \frac{1}{\text{jet\_AntiKt6Topo\_EMJES}}$ are fitted with Gaussian. The statistical mean and Gaussian mean are then plotted to confirm the Gaussian nature of the distributions as shown in Figure 5.24 for the first p_T region. The gaussian fit for the other two p_T regions are shown in Appendix B. For finding the resolution , the width of the Gaussian is plotted for $A_{Calibrated}$ and $A_{EMSCALE}$.

Figure 5.25 through 5.27, show the distribution of Asymmetry for Calibrated Jet `jet_AntiKt6Topo_pt` and uncalibrated jet `jet_AntiKt6Topo_emscale_pt`. The Correction factor $1 - \frac{1}{\text{jet\_AntiKt6Topo\_EMJES}}$ is also plotted. From the figure, the Asymmetry looks quite good with the calibrations (JES and ITC calibrations) working fine. The Asymmetry does not show any variations in the ITC region and looks quite flat as expected. The Asymmetry of both the calibrated and uncalibrated jets overlap each other with very little difference between the two. The reason for this being the same correction is applied to both the jets, the central jet and the free jet..

Figure 5.28 through 5.30 , compare the resolution of the calibrated and uncalibrated jets. As is seen in the figures, with calibration the resolution improves and goes down. The Asymmetry and Asymmetry resolution for higher p_T Jets show profound irregularity. In the region $2.0 < \eta < 2.8$, fluctuations in Asymmetry and Asymmetry resolution is quite high as well.

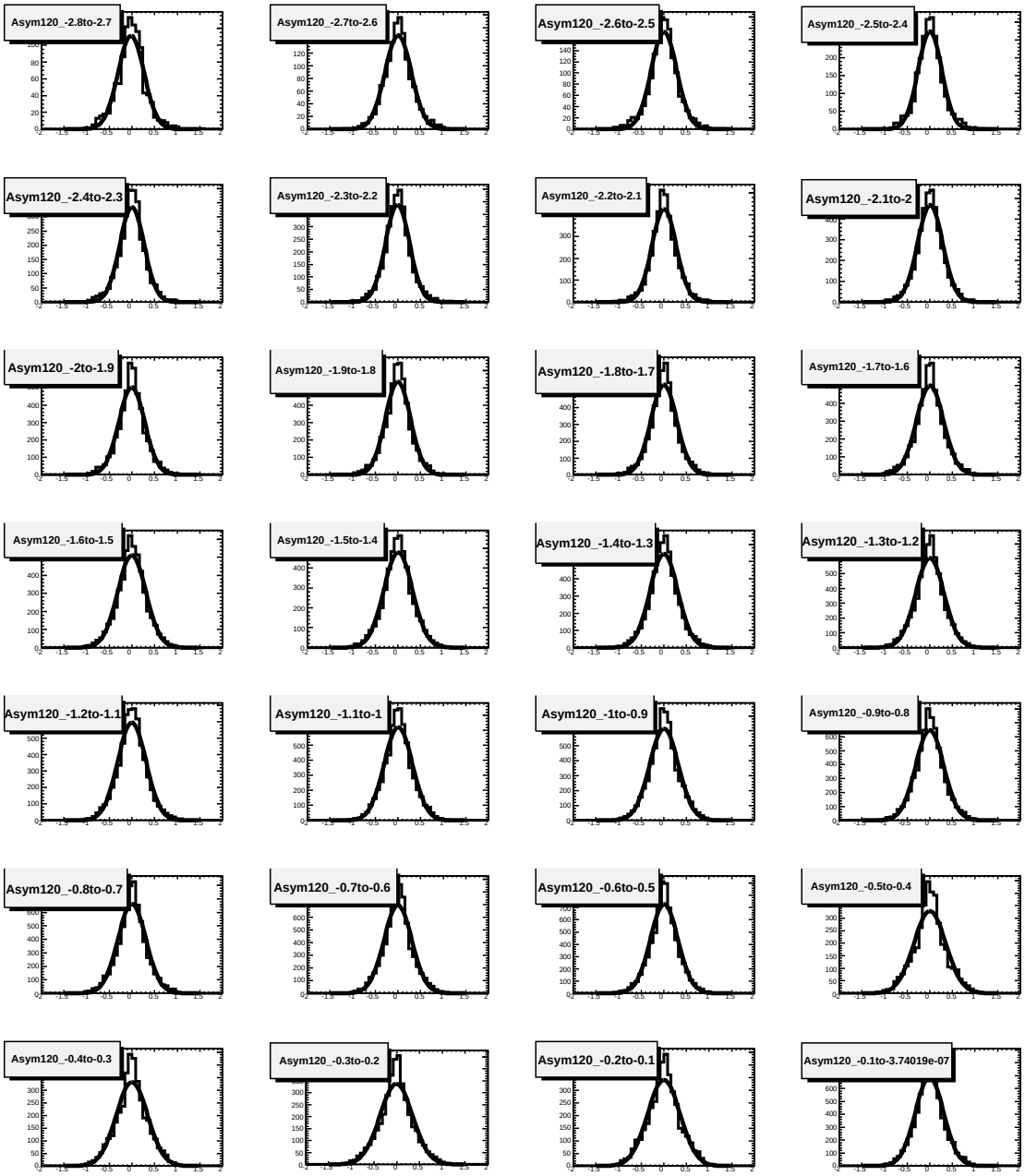

Figure 5.24. Calibrated Jet Asymmetry Fit at each η bin for Central Jet p_T in range $120GeV \leq p_T \leq 200GeV$.

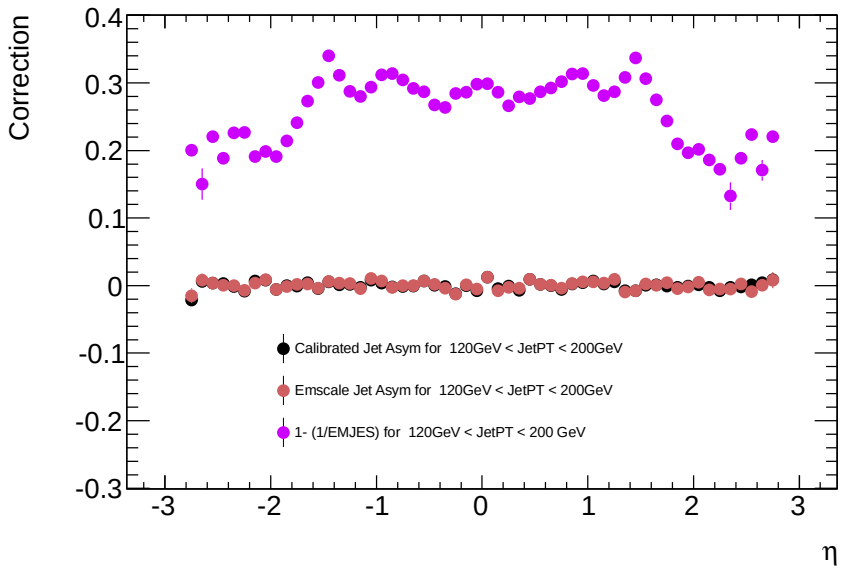

Figure 5.25. Mean of Asymmetry of Calibrated and Uncalibrated Jets and the distribution of correction factor $1 - \frac{1}{EMJES}$. The plots are for Central Jet p_T in range $120GeV \leq p_T \leq 200GeV$.

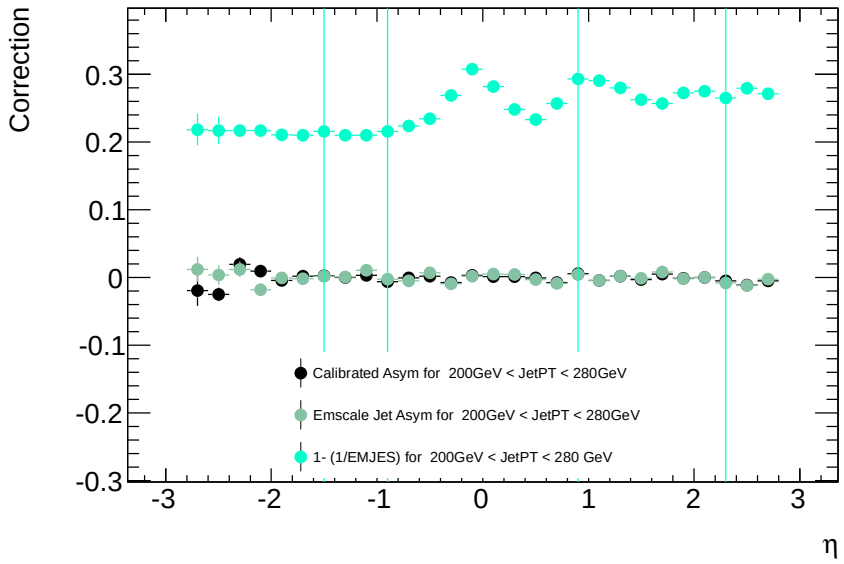

Figure 5.26. Mean of Asymmetry of Calibrated and Uncalibrated Jets and the distribution of correction factor $1 - \frac{1}{EMJES}$. The plots are for Central Jet p_T in range $200GeV \leq p_T \leq 280GeV$.

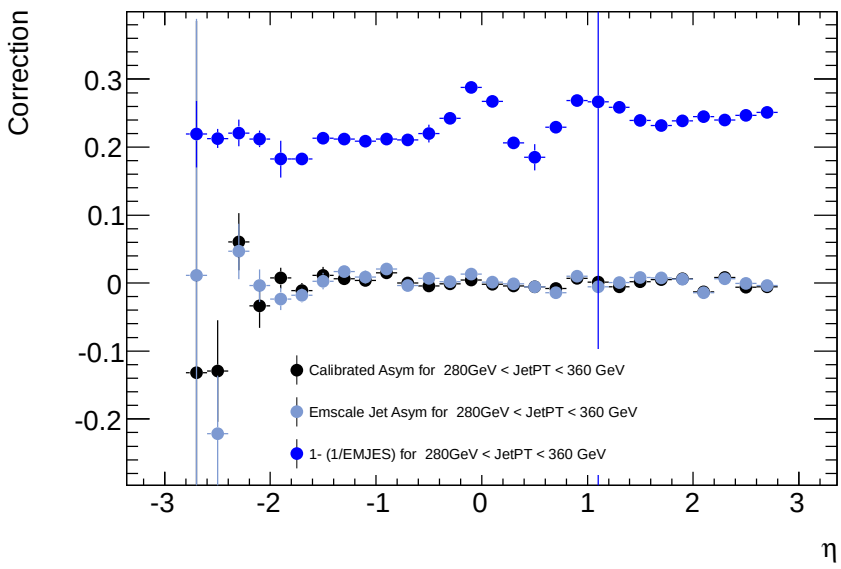

Figure 5.27. Mean of Asymmetry of Calibrated and Uncalibrated Jets and the distribution of correction factor $1 - \frac{1}{EMJES}$. The plots are for Central Jet p_T in range $280GeV \leq p_T \leq 360GeV$.

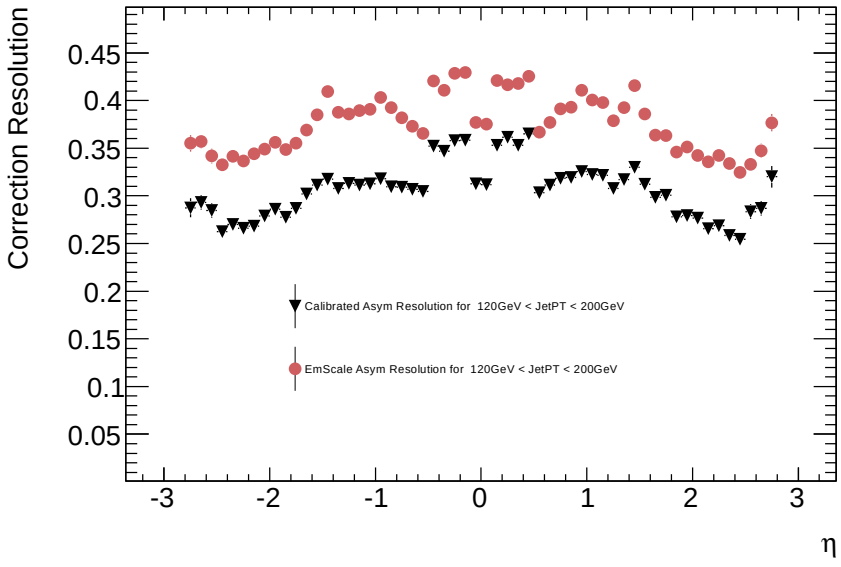

Figure 5.28. Resolution of Asymmetry of Calibrated and Uncalibrated Jets. The plots are for Central Jet p_T in range $120GeV \leq p_T \leq 200GeV$.

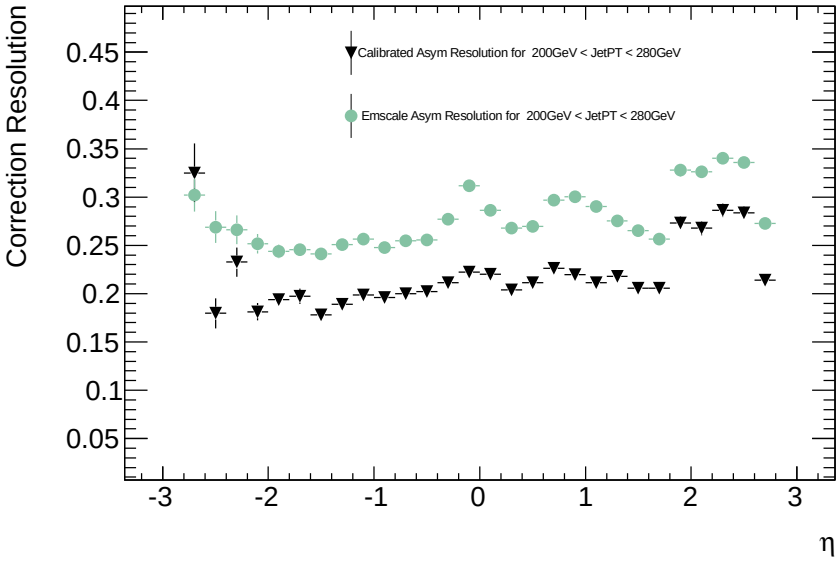

Figure 5.29. Resolution of Asymmetry of Calibrated and Uncalibrated Jets. The plots are for Central Jet p_T in range $200GeV \leq p_T \leq 280GeV$.

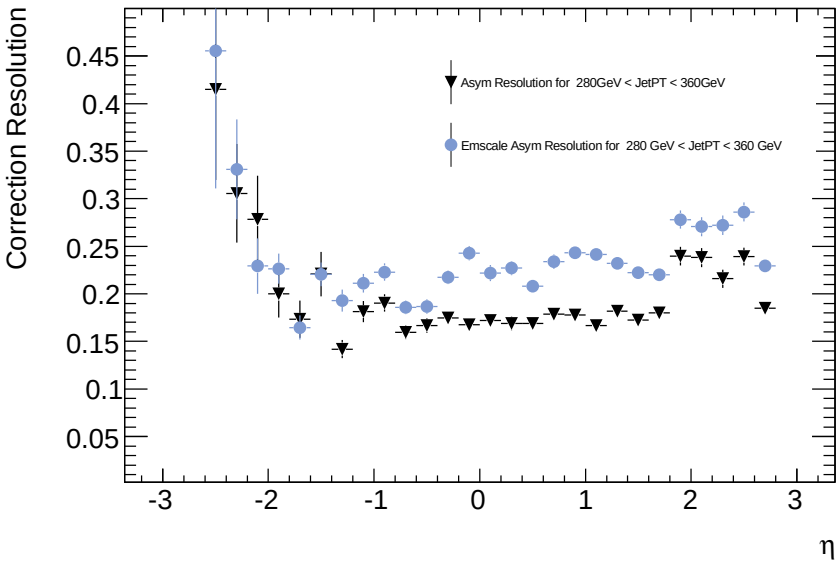

Figure 5.30. Resolution of Asymmetry of Calibrated and Uncalibrated Jets. The plots are for Central Jet p_T in range $280GeV \leq p_T \leq 360GeV$.

CHAPTER 6

CONCLUSION

In this dissertation, I have tried to briefly outline the ATLAS detector with all its sub-detectors and trigger systems. A brief description of reconstruction of various Physics objects have been given with a detailed illustration of Jets and Missing Transverse Energy.

The analysis was done to check Jet calibrations and Missing Transverse Energy Resolutions for dijet Events. The analysis concentrated on the study at the Central region of the detector with emphasis at the ITC region. The ITC is the sub-section of TileCal lying in the gap region of the long barrel and extended barrel. UTA has been involved in the design, installation, calibration and performance of the ITC cells. This dissertation emphasizes using real collision 7 TeV data to check the Missing Transverse Energy and Jet performance and calibration of the ITC region.

The calibrations and the Asymmetry variable are studied for the calibrated and uncalibrated jet. The resolution of the Asymmetry for both the Calibrated and uncalibrated jets are compared. All the studies were done for three different p_T regions across the η range. This helped in analyzing the Calorimeter and ITC performance better. The calibrations for ITC works well, with the Asymmetry quite good. There seems almost nominal deviation of Asymmetry in the ITC region with no non-linearity. Also with the calibrations both of ITC and EMJES, there is significant improvement in the resolution. The Missing Transverse Energy has also been studied in details for all the three PT regions across the η range. For higher Jet p_T range,there are higher missing transverse energy. The resolution of both the components of E_T^{miss}

deteriorates with p_T and in ITC regions. Also the E_x^{miss} fluctuates between $+veE_x^{miss}$ and $-veE_x^{miss}$.

Since the Jet response is almost flat, E_T^{miss} can not be improved. Further studies need to be done on this line. The Jet Asymmetry resolution needs to be improved. For the region of $-2.0 < \eta < -2.8$, for high p_T the Asymmetry resolution deteriorates. There is further scope of study for the improvement of Asymmetry resolution

APPENDIX A

GAUSSIAN FIT OF MET

Following are the figures for gaussian fit for E_x^{miss} and E_y^{miss} for the three p_T regions

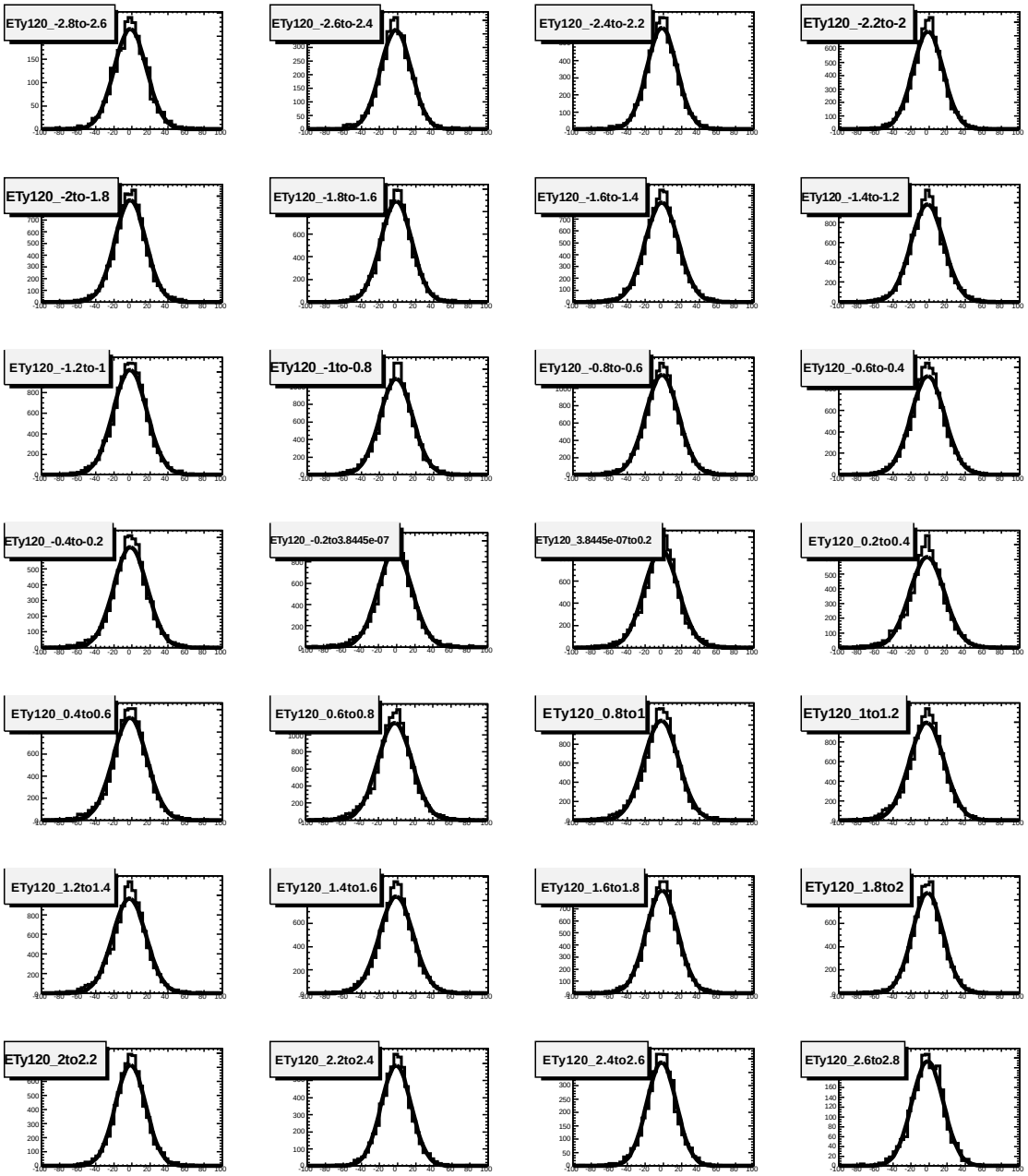

Figure A.1. Gaussian Fit of E_y^{miss} at each η bin for Central Jet p_T in range $120GeV \leq p_T \leq 200GeV$.

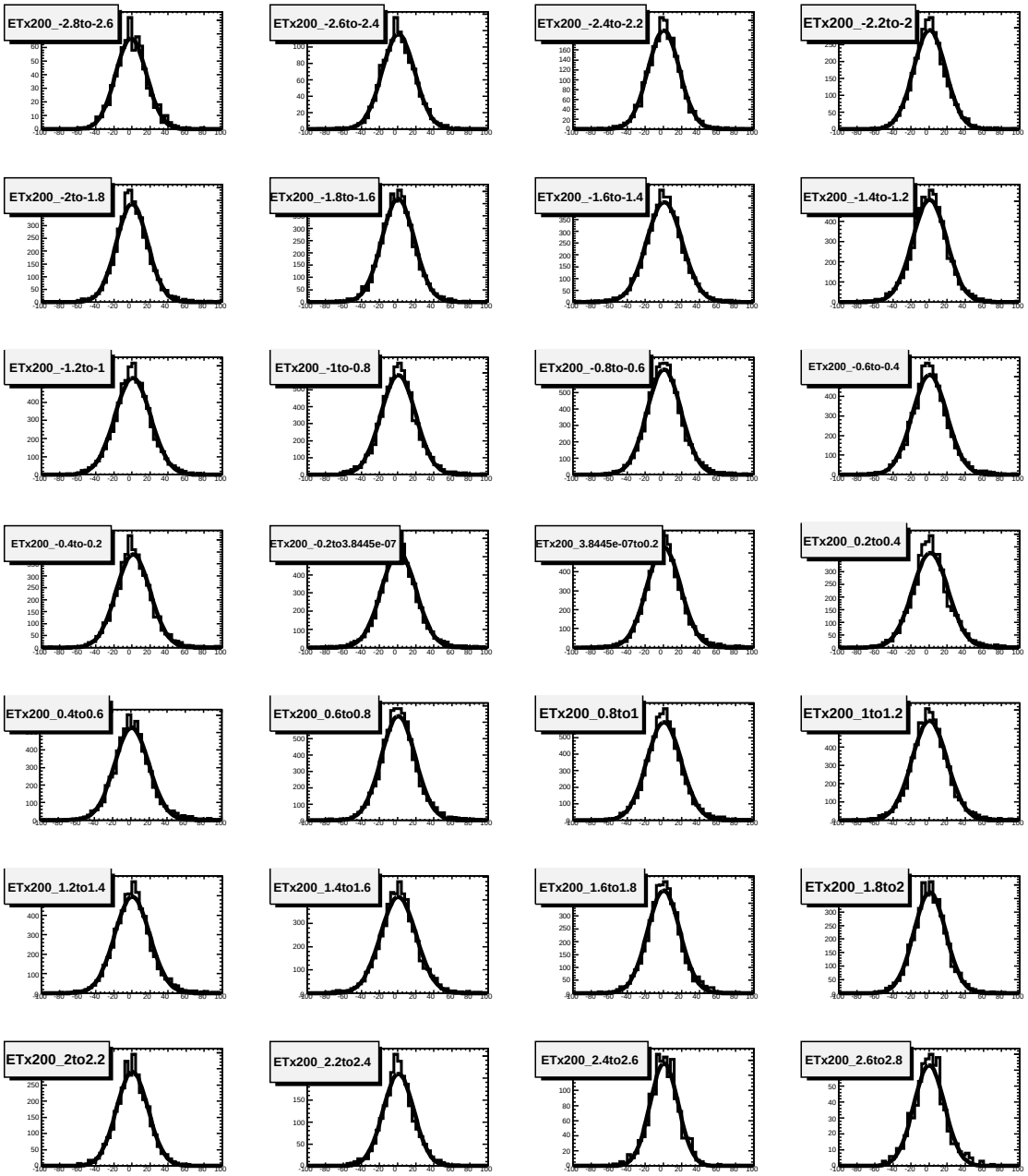

Figure A.2. Gaussian Fit of E_x^{miss} at each η bin for Central Jet p_T in range $200GeV \leq p_T \leq 280GeV$.

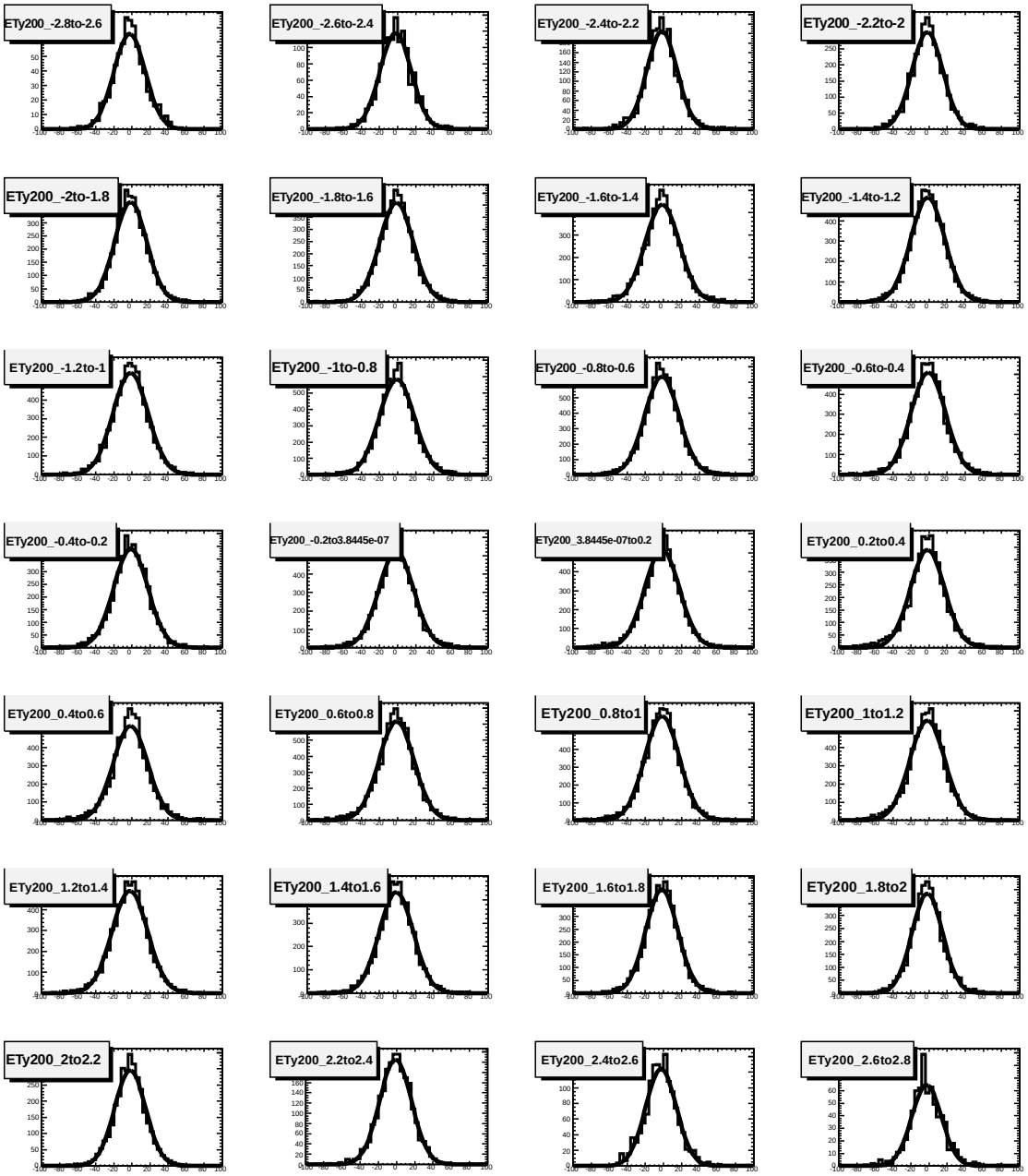

Figure A.3. Gaussian Fit of E_y^{miss} at each η bin for Central Jet p_T in range $200GeV \leq p_T \leq 280GeV$.

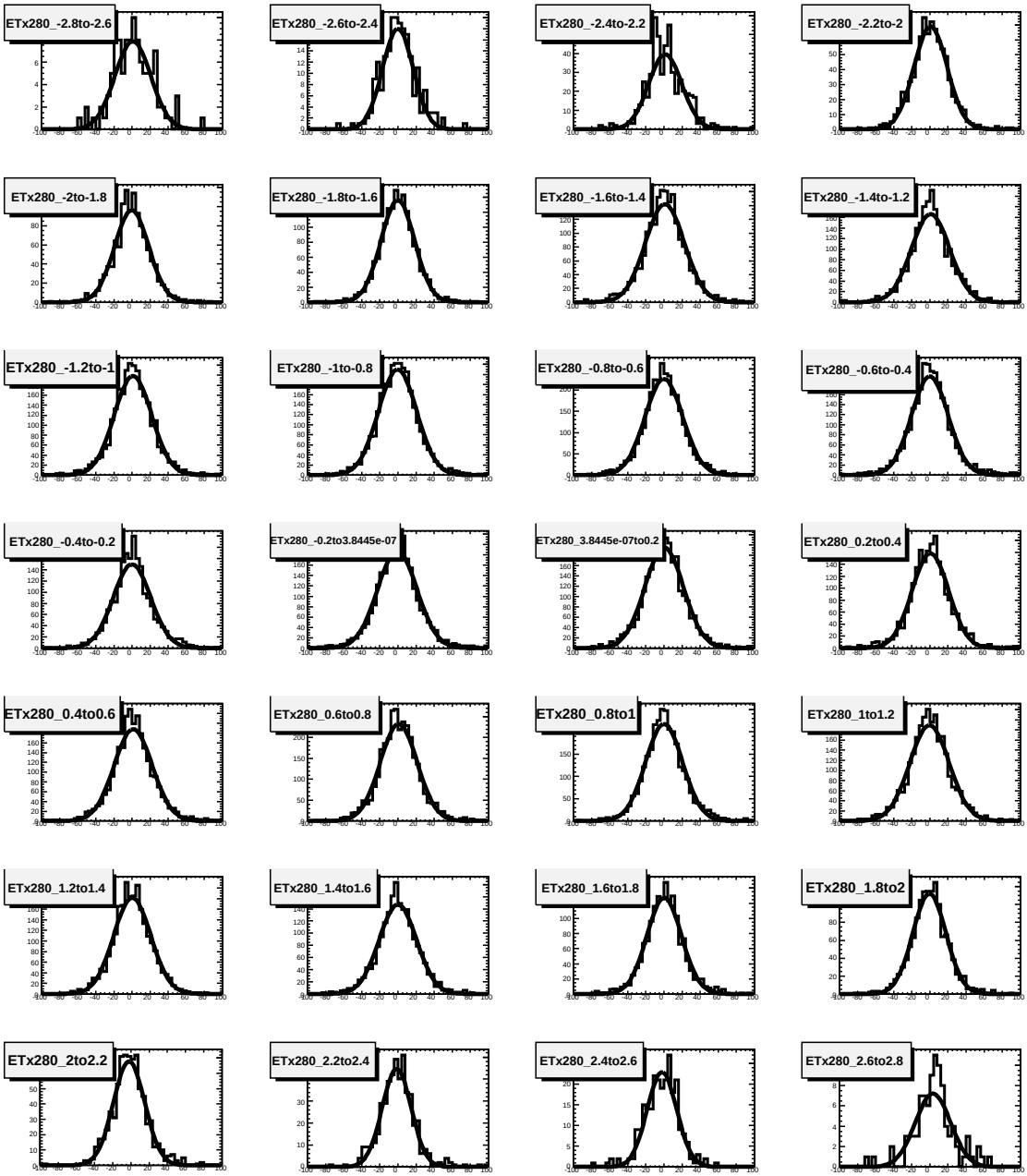

Figure A.4. Gaussian Fit of E_x^{miss} at each η bin for Central Jet p_T in range $280GeV \leq p_T \leq 360GeV$.

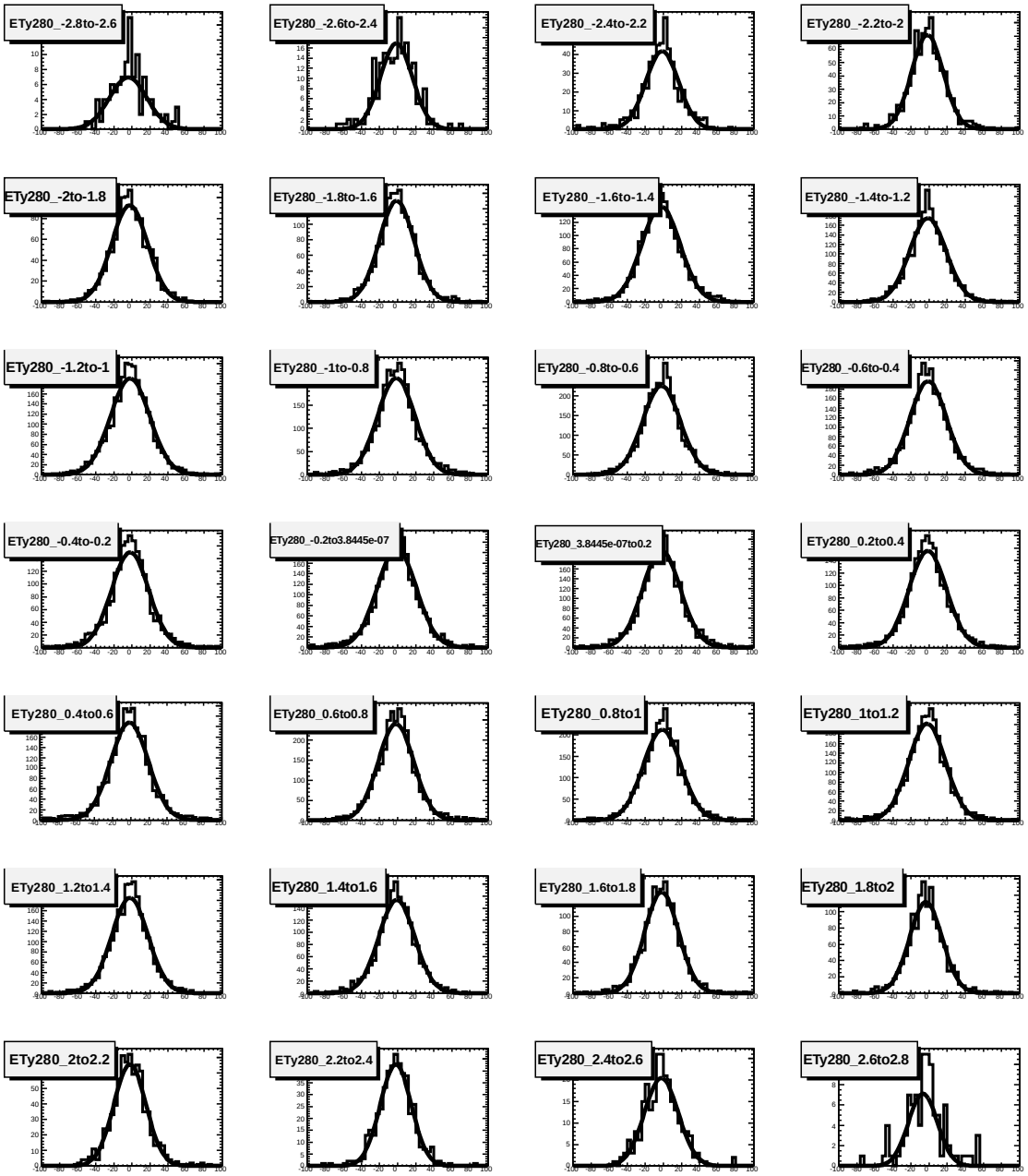

Figure A.5. Gaussian Fit of E_y^{miss} at each η bin for Central Jet p_T in range $280GeV \leq p_T \leq 360GeV$.

APPENDIX B

GAUSSIAN FIT OF ASYMMETRY VARIABLE

Following are the figures for gaussian fit for the Asymmetry variable for the remaining two p_T regions

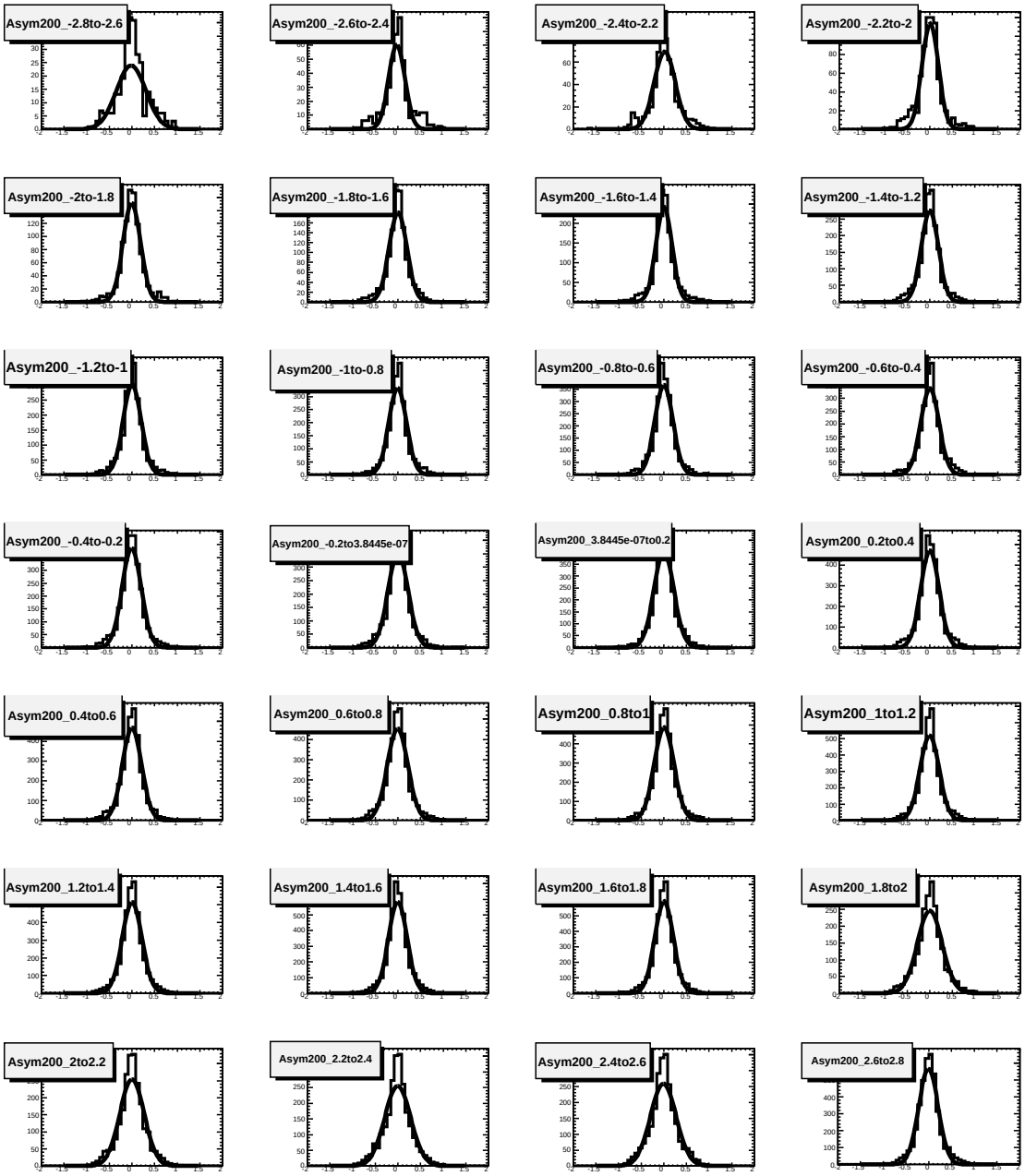

Figure B.1. Calibrated Jet Asymmetry Fit at each η bin for Central Jet p_T in range $200GeV \leq p_T \leq 280GeV$.

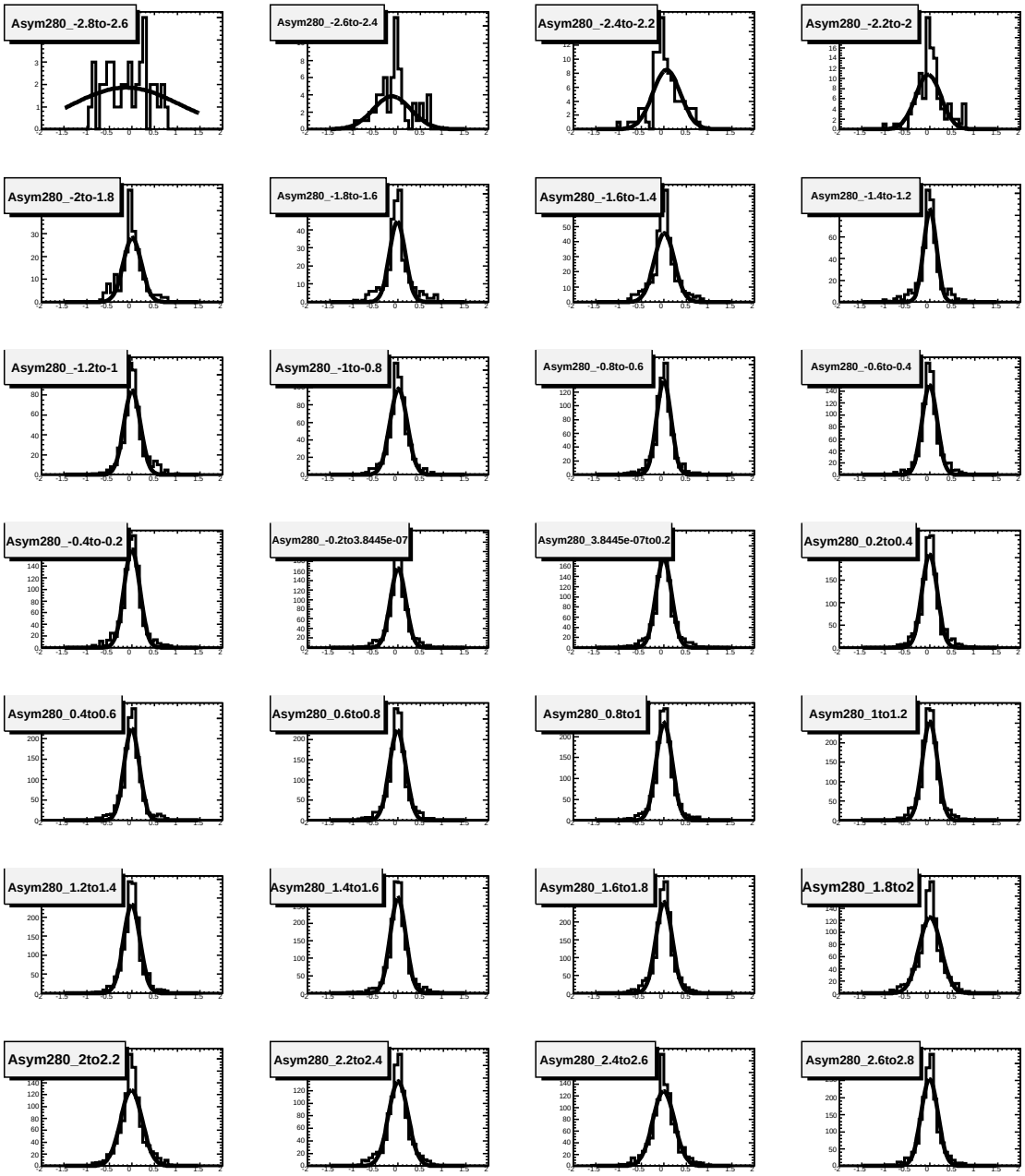

Figure B.2. Calibrated Jet Asymmetry Fit at each η bin for Central Jet p_T in range $280GeV \leq p_T \leq 360GeV$.

REFERENCES

[1] G. Aad *et al.*, "The ATLAS Experiment at the CERN Large Hadron Collider," *JINST*, vol. 3, p. S08003, 2008.

[2] C. Medina, "Analysis of calorimeter/itc cosmic ray data from the atlas detector,and preparation for supersymmetry searches," May 2009.

[3] S. B. et.al, "Measurement of inclusive jet and dijet production in pp collisions at p $\sqrt{s} = 7$ tev using the atlas detector (supporting documentation)," Tech. Rep., 2011.

[4] M. K. Gaillard, P. D. Grannis, and F. J. Sciulli, "The standard model of particle physics," 1999. [Online]. Available: doi:10.1103/RevModPhys.71.S96

[5] S. L. Glashow, "Partial Symmetries of Weak Interactions," *Nucl. Phys.*, vol. 22, 1961.

[6] A. Salam, "Weak and electromagnetic interactions," in *Elementary particle theory*, N. Svartholm, Ed. Almquist & Wiksell, 1968, pp. 367–377.

[7] A. Grau, G. Pancheri, and Y. N. Srivastava, "Hadronic total cross-sections through soft gluon summation in impact parameter space," *Phys. Rev. D*, vol. 60, no. hep-ph/9905228. LNF-99-010-P. UG-FT-99. 11, p. 114020. 20 p, May 1999.

[8] A. Moraes, C. Buttar, and I. Dawson, "Prediction for minimum bias and the underlying event at LHC energies," *The European Physical Journal C - Particles and Fields*, vol. 50, no. 2, pp. 435–466, Apr. 2007. [Online]. Available: http://dx.doi.org/10.1140/epjc/s10052-007-0239-1

[9] O. S. Brning, P. Collier, P. Lebrun, S. Myers, R. Ostojic, J. Poole, and P. Proudlock, *LHC Design Report*. Geneva: CERN, 2004.

[10] A. Collaboration, B. Alessandro, *et al.*, "Alice: Physics performance report, volume ii," *Journal of Physics G: Nuclear and Particle Physics*, vol. 32, no. 10, p. 1295, 2006. [Online]. Available: http://stacks.iop.org/0954-3899/32/i=10/a=001

[11] *CMS Physics Technical Design Report Volume I: Detector Performance and Software*, ser. Technical Design Report CMS. Geneva: CERN, 2006.

[12] "LHCb TDR computing technical design report," 2005.

[13] "ATLAS inner detector: Technical design report. Vol. 2," cERN-LHCC-97-17.

[14] A. Airapetian *et al.*, "ATLAS calorimeter performance Technical Design Report," 1996.

[15] *ATLAS liquid-argon calorimeter: Technical Design Report*, ser. Technical Design Report ATLAS. Geneva: CERN, 1996.

[16] D. M. Gingrich, "Construction, assembly and testing of the atlas hadronic endcap calorimeter," *Journal of Instrumentation*, vol. 2, no. 05, p. P05005, 2007.

[17] *ATLAS tile calorimeter: Technical Design Report*, ser. Technical Design Report ATLAS. Geneva: CERN, 1996.

[18] CERN. (2010, Nov.) Intermediate tile calorimeter. [Online]. Available: https://twiki.cern.ch/twiki/bin/viewauth/AtlasSandboxProtected/UtaItc/

[19] *ATLAS muon spectrometer: Technical Design Report*, ser. Technical Design Report ATLAS. Geneva: CERN, 1997, distribution.

[20] *Atlas Computing: technical design report.* Geneva: CERN, 2005.

[21] *ATLAS level-1 trigger: Technical Design Report*, ser. Technical Design Report ATLAS. Geneva: CERN, 1998.

[22] "ATLAS DAQ, EF, LVL2 and DCS: Technical progress report," cERN-LHCC-98-16.

[23] CERN. (2011, Jul) Electron reconstruction. [Online]. Available: https://twiki.cern.ch/twiki/bin/view/AtlasProtected/ElectronReconstruction/

[24] ——. (2011, Mar) Electron identification. [Online]. Available: https://twiki.cern.ch/twiki/bin/view/AtlasProtected/ElectronIdentification/

[25] ——. (2011, Nov) Muon combined reconstruction. [Online]. Available: https://twiki.cern.ch/twiki/bin/view/AtlasProtected/MuonPerformance/

[26] "A muon identification and combined reconstruction procedure for the atlas detector at the lhc at cern," Oct 2003, revised version number 1 submitted on 2003-10-30 18:34:15.

[27] G. P. Salam and G. Soyez, "A practical Seedless Infrared-Safe Cone jet algorithm," *JHEP*, vol. 05, p. 086, 2007.

[28] G. C. Blazey, J. R. Dittmann, S. D. Ellis, V. D. Elvira, K. Frame, S. Grinstein, R. Hirosky, R. Piegaia, H. Schellman, R. Snihur, V. Sorin, and D. Zeppenfeld, "Run ii jet physics: Proceedings of the run ii qcd and weak boson physics workshop," 2000. [Online]. Available: http://www.citebase.org/abstract?id=oai:arXiv.org:hep-ex/0005012

[29] S. Catani, Y. L. Dokshitzer, M. H. Seymour, and B. R. Webber, "Longitudinally invariant K(t) clustering algorithms for hadron hadron collisions," *Nucl. Phys.*, vol. B406, pp. 187–224, 1993.

[30] Y. L. Dokshitzer, G. D. Leder, S. Moretti, and B. R. Webber, "Better Jet Clustering Algorithms," *JHEP*, vol. 08, p. 001, 1997.

[31] M. Cacciari, G. P. Salam, and G. Soyez, "The anti-k_t jet clustering algorithm," 2008. [Online]. Available: doi:10.1088/1126-6708/2008/04/063

[32] "Jet energy scale and its systematic uncertainty in atlas for jets produced in proton-proton collisions at $sqrts = 7$ tev," CERN, Geneva, Tech. Rep. ATLAS-COM-CONF-2010-058, Jun 2010, (Was originally 'ATL-COM-PHYS-2010-404').

[33] CERN. (2011, Nov) Jet calibration. [Online]. Available: https://twiki.cern.ch/twiki/bin/view/AtlasProtected/JetCalibration/

[34] ——. (2010) Missing transverse energy. [Online]. Available: https://twiki.cern.ch/twiki/bin/view/AtlasProtected/EtMiss/

[35] W. Lampl, S. Laplace, D. Lelas, P. Loch, H. Ma, S. Menke, S. Rajagopalan, D. Rousseau, S. Snyder, and G. Unal, "Calorimeter clustering algorithms: Description and performance," CERN, Geneva, Tech. Rep. ATL-LARG-PUB-2008-002. ATL-COM-LARG-2008-003, Apr 2008.

[36] M. Baak, M. Petteni, and N. Makovec, "Data-quality requirements and event cleaning for jets and missing transverse energy reconstruction with the atlas detector in proton-proton collisions at a center-of-mass energy of $sqrts = 7$ tev," CERN, Geneva, Tech. Rep. ATLAS-COM-CONF-2010-038, May 2010, (Was originally 'ATL-COM-PHYS-2010-247').

[37] "Measurement of missing tranverse energy," CERN, Geneva, Tech. Rep. ATL-PHYS-PUB-2009-016. ATL-COM-PHYS-2009-118, Mar 2009, draft PUB Note for 'Measurement of Missing Transverse Energy in ATLAS' Chapter (J13).

[38] CERN. Data quality summary. [Online]. Available: https://atlas.web.cern.ch/Atlas/GROUPS/DATAPREPARATION/DQSummary/

[39] K. Prokofiev, G. Piacquadio, and A. Wildauer, "First performance results of primary vertex reconstruction in proton-proton collisions at 7 tev," CERN, Geneva, Tech. Rep. ATLAS-COM-CONF-2010-070, Jun 2010, (Was originally 'ATL-COM-PHYS-2010-418').

[40] CERN. (2011, Oct) How to clean jets. [Online]. Available: https://twiki.cern.ch/twiki/bin/viewauth/AtlasProtected/HowToCleanJets/

[41] ——. (2011, Oct) Jet energy scale. [Online]. Available: https://twiki.cern.ch/twiki/bin/viewauth/AtlasProtected/JetEnergyScale/

BIOGRAPHICAL STATEMENT

Sushmita Sahu was born in Kolkata, India in 1981. She received her B.E. in Telecommunication Engineering in the year 2003 from Rajiv Gandhi Technical University, Bhopal, India. From 2005-2009. she worked as a Software Engineer in Infosys Technologies Ltd., India. In Fall 2011, she received her Master's Degree in Physics from University of Texas at Arlington. During her graduate research, she has worked with the High Energy Physics(HEP) group at UTA.